ARTICLE

Divalent *closo*-monocarborane solvates for solid-state ionic conductors.

Received 00th January 20xx,
Accepted 00th January 20xx

DOI: 10.1039/x0xx00000x

Amanda Berger, [a] Ainee Ibrahim, [a] Craig E. Buckley, [a] and Mark Paskevicius.[a]

Li-ion batteries have held the dominant position in battery research for the last 30+ years. However, due to inadequate resources and the cost of necessary elements (e.g., lithium ore) in addition to safety issues concerning the components and construction, it has become more important to look at alternative technologies. Multivalent metal batteries with solid-state electrolytes are a potential option for future battery applications. The synthesis and characterisation of divalent hydrated *closo*-monocarborane salts; $Mg[CB_{11}H_{12}]_2{\cdot}xH_2O$, $Ca[CB_{11}H_{12}]_2{\cdot}xH_2O$, and $Zn[CB_{11}H_{12}]_2{\cdot}xH_2O$; have shown potential as solid-state electrolytes. The coordination of a solvent (e.g. H_2O) to the cation in these complexes shows a significant improvement in ionic conductivity, i.e. for $Zn[CB_{11}H_{12}]_2{\cdot}xH_2O$ dried at 100 °C (10^{-3} S cm^{-1} at 170 °C) and dried at 150 °C (10^{-5} S cm^{-1} at 170 °C). Solvent choice also proved important with the ionic conductivity of $Mg[CB_{11}H_{12}]_2{\cdot}3en$ (en = ethylenediamine) being higher than $Mg[CB_{11}H_{12}]_2{\cdot}3.1H_2O$ (2.6×10^{-5} S cm^{-1} and 1.7×10^{-8} S cm^{-1} at 100 °C, respectively), however, the oxidative stability was lower (<1 V (Mg^{2+}/Mg) and 1.9 V (Mg^{2+}/Mg), respectively). Thermal characterisation of the divalent *closo*-monocarborane salts showed melting and desolvation, prior to high temperature decomposition.

Introduction

Lithium-ion (Li-ion) batteries have dominated the energy storage market since the early 1990's due to their excellent gravimetric energy capacity and high cell potential. As society moves towards renewable energy resources, such as solar and wind, it is important to continue developing better, more efficient, and cost-effective battery technologies to provide base-load renewable power. This is also important for the future adoption of long-range electric vehicles. However, the future of Li-ion batteries has become an issue due to the increasingly high cost and debated shortage of lithium and other rare elements such as cobalt that are needed for battery fabrication.[1–3] Safety concerns, due to the use of volatile carbonate solvents typically used in Li-ion batteries, or metal dendrite growth, has also played a role in the movement toward developing alternative battery technologies.

One alternative to Li-ion batteries is the development of multivalent metal batteries, consisting of metals such as magnesium (Mg^{2+}), calcium (Ca^{2+}), zinc (Zn^{2+}), and aluminium (Al^{3+}).[4–6] These systems can benefit from the use of metal anodes, whereas current Li-ion batteries are limited to intercalating anodes such as graphite (see Table 1). Hence, multivalent metal batteries thus offer a significant potential increase in energy density and lower cost. Comparatively, a pure lithium metal anode has the highest gravimetric capacity, however, practical use has been limited due to irregular lithium plating during cycling processes causing severe dendrite growth, which consequently can lead to short circuiting of the cell.[7] In comparison, metals like magnesium and calcium are less prone to dendrite growth, as well as having the added benefit of being some of the most abundant elements on earth, and consequently, less expensive and more accessible than lithium.[7–9] Calcium and magnesium have similar reduction potentials to lithium for a single-electron transfer, however, as these compounds form divalent cations ($M \rightarrow M^{2+} + 2e^-$), this doubles the theoretical gravimetric energy capacity of the pure metal anode. Significant work has been performed on the development of non-aqueous electrolytes for magnesium based batteries. For example, magnesium bis(triflurometh anesulfonyl)imide ($Mg(TFSI)_2$), is one of the ether-soluble magnesium salts that has been thoroughly investigated.[10,11] In dimethoxyethane (DME), $Mg(TFSI)_2$ showed poor reversibility in Mg plating, however the addition of magnesium chloride ($MgCl_2$) improved reversibility considerably.[11] Unfortunately, chloride anions are corrosive, therefore, non-aqueous chloride-free Mg electrolytes, such as a perfluorinated pinacolate-coordinated borate salt ($Mg[B(O_2C_2(CF_3)_4)_2]$) or magnesium *closo*-monocarbadodecaborate ($Mg[CB_{11}H_{12}]_2$), are also being developed.[12] $Mg[CB_{11}H_{12}]_2$ salts have been investigated as potential liquid electrolytes in the form of ionic salts dissolved in various glycol diether solvents such as; DME, diglyme, and tetraglyme; displaying excellent oxidative stability in

[a] *Department of Physics and Astronomy, Curtin University, GPO Box U1987, Perth, WA 6845, Australia.*

† Electronic Supplementary Information (ESI) available: Full characterisation including ^{1}H, ^{11}B, ^{11}B{^{1}H} NMR, FTIR, Raman and XRD for $Mg[CB_{11}H_{12}]_2{\cdot}xH_2O$, $Ca[CB_{11}H_{12}]_2{\cdot}xH_2O$ and $Zn[CB_{11}H_{12}]_2{\cdot}xH_2O$. It also includes the characterisation including ^{1}H, ^{11}B, ^{11}B{^{1}H} ^{13}C{^{1}H} HSQC NMR, and FTIR for $Mg[CB_{11}H_{12}]_2$ and $Mg[CB_{11}H_{12}]_2{\cdot}3en$. ^{1}H, ^{11}B, ^{11}B{^{1}H} NMR has also been shown for $Ca[B_{12}H_{12}]$, $Zn[CB_{11}H_{12}]$, mixed $Zn[B_{12}H_{12}]$ + $Zn[CB_{11}H_{12}]_2$, and $Me_3NH[12\text{-}OH\text{-}CB_{11}H_{11}]$. Ionic conductivities of mixed $Zn[B_{12}H_{12}]$ + $Zn[CB_{11}H_{12}]_2$, Nyquist plots and i*n situ* SR-XRD showing the decomposition of $Mg[CB_{11}H_{12}]_2{\cdot}3en$ have also been included. See DOI: 10.1039/x0xx00000x

comparison to alternatives such as $Mg(TFSI)_2$.[10,13] Calcium *closo*-monocarbadodecaborate ($Ca[CB_{11}H_{12}]_2$) in a mixture of equal volumes of THF/DME, showed discharge and charge capacities of 805 mAh g^{-1} and 750 mAh g^{-1}, respectively, indicating compatibility in a Ca-S battery.[14]

Whilst there is promising research into the development of non–aqueous multivalent batteries, alternatively, solid-state electrolytes have risen in prominence for potential future batteries. Much of the investigation into solid-state batteries has focused on group 1 alkali metal salts, particularly lithium. This includes solid inorganic electrolytes, e.g., LISICON, NASICON, argyrodite, garnet, perovskite, Li-hydride, and polyhydroborate salts.[15–19] Solid-state magnesium electrolytes have also been proposed with similar structures to that of common lithium and sodium solid electrolytes. Ceramic and glass type magnesium solid-state electrolytes have potential, however, many including NASICON-type $Mg_{0.5}Zr_2(PO_4)_3$ or $(Mg_{0.1}Hf_{0.9})_{4/3.8}Nb(PO_4)_3$ only have sufficient ionic conductivities at elevated temperatures (~10^{-5} S cm^{-1} at 400 °C and ~10^{-6} S cm^{-1} at 300 °C, respectively) that are not appropriate for most battery applications.[20,21] Magnesium borohydride ($Mg(BH_4)_2$) compounds have also been investigated and modified to improve ionic conductivity at temperatures closer to room temperature.[22–26] On its own, $Mg(BH_4)_2$ has low ionic conductivity at ambient temperature (~10^{-12} S cm^{-1}) and is still not viable at higher temperatures (10^{-9} S cm^{-1} at 150 °C).[26,27] By ball-milling $Mg(BH_4)_2$ and annealing with $Mg(NH_2)_2$ at 120 °C, the ionic conductivity was improved in the solid-state (4×10^{-5} S cm^{-1} at 100 °C).[23] However, chelation of different solvents has also been shown to improve the ambient temperature (30 °C) ionic conductivity; e.g., $Mg(en)_3(BH_4)_2$ and $Mg(en)(BH_4)_2$ (where en = ethylenediamine) with ionic conductivities of ~10^{-10} and ~10^{-7} S cm^{-1}, respectively.[26] The addition of ammonia borane via mechanical milling with $Mg(BH_4)_2$ further improved ionic conductivity to 1×10^{-5} S cm^{-1} at 25 °C via the formation of $Mg(BH_4)_2(NH_3BH_3)_2$.[25]

Solid-state electrolytes for calcium, aluminium, and zinc solid-state batteries are less extensively researched compared to those for magnesium. For calcium, NASICON-type $(Ca_{0.05}Hf_{0.95})_{4/3.9}Nb(PO_4)_3$ and $CaZr_4(PO_4)_6$ have ionic conductivities of 5×10^{-5} S cm^{-1} at 600 °C and 1.4×10^{-6} S cm^{-1} at 800 °C, respectively.[28,29] For Zn, one example is $ZnZr_4(PO_4)_6$, which like $CaZr_4(PO_4)_6$, demonstrates practical ionic conductivity only at higher temperatures (~10^{-6} S cm^{-1} at 500 °C).[30] $ZnPS_3$, an inorganic solid, was found to have an ionic conductivity of ~10^{-8} – 10^{-6} S cm^{-1} at 60 °C, with this uncertainty attributed to differences in the Zn-$ZnPS_3$ interface.[31] Alternatively, polymer-type 'pseudo' solid-state electrolytes with high ionic conductivity have also been analysed, with a significant proportion dedicated to multivalent polymer electrolytes.[32–40] Prolific research has been undertaken in the development of zinc-aqueous polymer electrolytes using cheap, flexible gelling agents; e.g., guar gum, xanthum gum, and gelatin; along with aqueous solutions of typically $ZnSO_4$, but more recently, $Zn(TFSI)_2$ (bis(trifluoromethane)sulfonimide) or $Zn(CF_3SO_3)_2$.[33,34,41] The larger, bulkier anions, particularly $CF_3SO_3^-$, have exhibited high cyclability during continuous charge and discharge cycles in addition to low polarisation and high coulombic efficiency compared to $ZnSO_4$-based electrolytes.[41]

In order to create a successful solid-state multivalent inorganic electrolyte, the investigation into novel compounds is important. While, as previously described, both non-aqueous $Mg[CB_{11}H_{12}]_2$ and $Ca[CB_{11}H_{12}]_2$ have been explored as possible ionic-liquid based electrolytes, little has been previously published about their solid-state ionic conductivity or thermal characteristics.[10,13,14,42] $LiCB_{11}H_{12}$ and $NaCB_{11}H_{12}$ have been thoroughly studied as potential solid- state electrolytes for batteries, and have demonstrated almost liquid-like ionic conductivity in the solid- state at higher temperatures, owing to polymorphic phase transitions into super ionic conductive salts.[43–45] These hydroborate salts have proven to be thermally

Table 1 Comparison of the properties of anodes for Li-intercalated graphite, Li, Na, Mg, Ca and Zn. The table shows a comparison of associated reduction potentials for single-electron transfers, anode, gravimetric and volumetric densities, abundance in earth's crust (ppm) and cost per metric ton of ore or metal (USD) have been presented.[7,46] Gravimetric energy capacity was calculated from the equation $Q = zF/M$ where z is the number of electrons transferred, F is the Faraday constant (26800 mAh mol^{-1}) and M is molar mass.[8] Cost of ore was sourced from the USGS 2022 mineral commodities report.[46] [a]Crystal density of graphite. [b] Theoretical gravimetric (and volumetric) capacity based of the density of un-lithiated graphite. Ore was presented as graphite flakes, [c]Li_2CO_3 (battery grade), [b]soda ash (Na_2CO_3), [e]metallic magnesium (Mg), [f]quick lime (CaO) and [g]metallic zinc (Zn).

	Graphite (Li-ion)	Lithium (Li)	Sodium (Na)	Magnesium (Mg)	Calcium (Ca)	Zinc (Zn)
Reduction Potential (V) vs. SHE	~-3	-3.04	-2.71	-2.37	-2.76	-0.76
Metal/crystal density (g cm^{-3})	2.27[a]	0.53	0.97	1.74	1.55	7.15
Gravimetric energy capacity (mAh g^{-1})	372[b]	3862	1166	2205	1337	820
Volumetric energy capacity (mAh cm^{-3})	843[b]	2062	1132	2832	2073	5845
Abundance in Earth's crust (ppm)	200	20	23600	23300	41500	70
Cost (USD/t)	~1500	17000[c]	155[d]	5500[e]	140[f]	2999[g]

stable; due to large, weakly-coordinating, and aromatically electron delocalised cage-like anions; with both lithium and sodium salts able to be dehydrated thermally during synthesis.[47,48] Of all of the hydroborate anions that have been analysed for solid-state electrolytes, the $[CB_{11}H_{12}]^-$ anion has showed increased oxidative stability in comparison to $[B_{10}H_{10}]^{2-}$, $[B_{12}H_{12}]^{2-}$, and $[CB_9H_{10}]^-$.[45,49,50] It has previously been noted that the synthesis of the $[CB_{11}H_{12}]^-$ anion is expensive, thus limiting its application in solid-state batteries.[51,52] However, recent advances have shown that there is an inexpensive route to synthesise the $[CB_{11}H_{12}]^-$ anion that utilises low-cost reagents.[53] The following paper explores the synthesis and thermal characteristics of $M[CB_{11}H_{12}]_2$ (where M = Mg^{2+}, Ca^{2+} and Zn^{2+}) to analyse their potential as multivalent carborane solid-state electrolytes.

Results and Discussion

Synthesis and characterisation

A variety of divalent *closo*-monocarboranes were synthesised so that their solid-state ionic conductivity and thermal properties could be investigated. The synthesis of divalent *closo*-monocarborane hydrates was undertaken by first dissolving $Me_3NH[CB_{11}H_{12}]$ (Trimethylammonium *closo*-monocarbadodecarborane) in a solution of aqueous NaOH followed by heating to 60 – 80 °C to remove trimethylamine gas. The resulting colourless solution was then cooled to room temperature and passed through an acidic ion exchange column to form the acidic carborane, $[H_3O][CB_{11}H_{12}]$. The clear acidic solution (pH < 1) was then neutralised with a divalent carbonate (or hydroxide) to form a soluble divalent *closo*-monocarborane hydrate (Ca, Mg, or Zn). After vacuum evaporation of the solution, the precipitates were further dried under vacuum at 100 °C for 16 hours, unless otherwise stated. All divalent metal salts, $Mg[CB_{11}H_{12}]_2{\cdot}xH_2O$, $Ca[CB_{11}H_{12}]_2{\cdot}xH_2O$, and $Zn[CB_{11}H_{12}]_2{\cdot}xH_2O$, were deliquescent white powders.

The water coordination to magnesium *closo*-monocarborane hydrate is of particular interest as previous literature surrounding the carbon-free analogue, $Mg[B_{12}H_{12}]{\cdot}xH_2O$, indicates that the salt undergoes hydroxylation along with dehydration at temperatures above 250 °C due to the magnesium cation's oxophilicity and bond formation between the boron-bound H^- and the H^+ of the water.[54,55] Mg^{2+} has a high charge density compared to alkali metals, such as Li^+ and Na^+, which can result in strong coordination of solvated water to the cation.[17] For comparison, the Li^+ and Na^+ $[CB_{11}H_{12}]^-$ salts can be fully dehydrated at temperatures of 160 °C and 80 °C respectively, for 6 hours.[43] Thus, $Mg[CB_{11}H_{12}]_2{\cdot}xH_2O$ was not dried at temperatures higher than 100 °C to avoid hydroxylation and/or decomposition.

In an attempt to synthesise unsolvated $Mg[CB_{11}H_{12}]_2$ and avoid the problems with dehydration of the magnesium *closo*-monocarborane, a water-free synthesis method was undertaken. Here, $Me_3NH[CB_{11}H_{12}]$ was reacted with an excess solution of *n*-dibutylmagnesium ($MgBu_2$) in hexane under argon

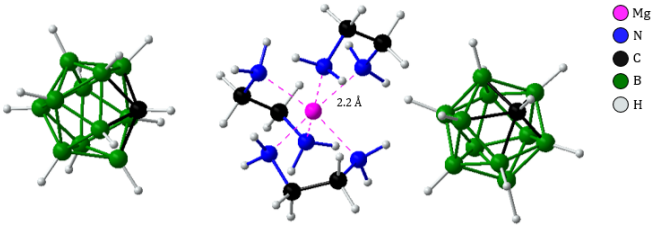

Figure 1 Crystal structure coordination of $Mg[CB_{11}H_{12}]_2{\cdot}3en$ showing $[CB_{11}H_{12}]^-$ anions and octahedrally coordinated $[Mg(en)_3]^{2+}$ clusters.

using Schlenk techniques. The resulting white powder was especially hygroscopic if exposed to air. A further derivative was also synthesised to investigate alternative solvation to Mg^{2+} by using ethylenediamine (en) rather than water. The addition of en to $Mg[CB_{11}H_{12}]_2$ was undertaken under argon, and after drying, a bright yellow powder remained as $Mg[CB_{11}H_{12}]_2{\cdot}3en$.

Characterisation of synthesised materials was performed using ^1H, ^{11}B, $^{11}B\{^1H\}$ and $^{13}C\{^1H\}$ nuclear magnetic resonance spectroscopy (NMR), Fourier transform infrared (FTIR) spectroscopy, Raman spectroscopy, and powder X-ray diffraction (pXRD) (Figures S1-S13). Analysis of ^1H NMR indicated that there was no remaining Me_3NH^+ present in the divalent salts from the loss of a resonance for $-CH_3$ at 2.6 – 2.7 ppm that was present for $Me_3NH[CB_{11}H_{12}]$ (Figure S1a). Water was also present in $Zn[CB_{11}H_{12}]{\cdot}xH_2O$ with a broad resonance at 2.9 ppm in anhydrous CD_3CN. ^{11}B NMR demonstrated the typical doublets at -7.0, -13.3 and -16.1 ppm that indicated the boron atoms of the cage with terminal hydrogen bonds to be in a 1:5:5 ratio.[53] However, some impurities were identified in ^{11}B NMR due to the presence of $B(OH)_3$ at ~20.0 ppm or $B(OH)_4^-$ at ~1.9 ppm (Figure S1b and S1c). It could be presumed that partial oxidation/decomposition of the cage occurred during synthesis causing impurities of $B(OH)_3/B(OH)_4^-$ in the final product. This could have occurred due to the synthetic environmental conditions; i.e., the low pH of the acid form of the carborane during cation exchange, the reaction of $[H_3O][CB_{11}H_{12}]$ with base, or from drying the product at high temperature. However, no other impurities were identified in the divalent salts.

For the synthesis of solvent-free $Mg[CB_{11}H_{12}]_2$, $MgBu_2$ was used to deprotonate the Me_3NH^+ cation. A similar reactant, diphenylmagnesium ($MgPh_2$), has been previously mixed with $Mg[CB_{11}H_{12}]_2$ in dimethoxyethane (DME), to form the soluble compound, $MgPh[CB_{11}H_{12}]$ in DME.[56] In the previous work, the use of an ethereal solvent, favoured the formation of the Grignard product (RMgX), unlike in the currently described reaction where hexane is a less coordinating solvent and drives the reaction in the direction of $Mg[CB_{11}H_{12}]_2$. ^1H NMR indicates that $MgBu_2$ was successful in deprotonating the Me_3NH^+ cation, with the absence of the 2.77 ppm resonance in the ^1H NMR spectra of $Mg[CB_{11}H_{12}]_2$, and only a small amount of residual butane was detected as an impurity (Figure S2a and S2b). However, there was a new resonance at 2.10 ppm in the $Mg[CB_{11}H_{12}]_2$ ^1H NMR that is believed to be residual trimethylamine (Me_3N) or potentially dimethylamine (Me_2NH) that may coordinate to the Mg^{2+} cation (Figure S2b). To confirm this, $^{13}C\{^1H\}$ NMR indicated that the resonance at 47.4 ppm was

an impurity, with ^{1}H-^{13}C HSQC demonstrating that this resonance correlated to the one at 2.10 ppm in ^{1}H NMR (Figures S2b, S5, and S6). Interestingly, this impurity was not observed in the ^{1}H NMR of $Mg[CB_{11}H_{12}]_2$·3en, having disappeared after the en solvate had formed, with a new broad resonance that overlapped with that of DMSO at 2.50 ppm, indicating the presence of ethylenediamine, which normally has a mode at 2.6 ppm in DMSO-*d6* (Figure S2c).[57] $^{13}C\{^{1}H\}$ NMR (DMSO-*d6*) of $Mg[CB_{11}H_{12}]_2$·3en shows a broad resonance that was attributed to the C-H of the boron cage at 50.9 ppm and another broad mode at 42.8 ppm that was assigned to the 3 ethylenediamine units coordinated to Mg^{2+} (Figure S7). Confirmation that three ethylenediamine are coordinated to Mg^{2+} was also obtained with SR-XRD through crystal structure determination as described below.

An estimation of water content was undertaken using thermogravimetric analysis (TGA) (Table S1). This can only be assumed to be an estimate because hydrolysis and decomposition of the cage occurred when the hydrated salts were heated under argon. This is described in further detail in the following section. The sample of $Mg[CB_{11}H_{12}]_2$·xH$_2$O dried to 100 °C was estimated to have 3.1 mol of water to each mole of $Mg[CB_{11}H_{12}]_2$, thus could be designated as $Mg[CB_{11}H_{12}]_2$·3.1H$_2$O. $Ca[CB_{11}H_{12}]_2$·xH$_2$O was dried at 100, 125 and 150 °C, however, TGA of the 150 °C sample was not performed. For the sample of $Ca[CB_{11}H_{12}]_2$·xH$_2$O dried at 100 °C, water content was estimated to be 1.9, whereas the sample dried at 125 °C was estimated to be <1 (0.8), thus, the designation for theses samples was $Ca[CB_{11}H_{12}]_2$·1.9H$_2$O and $Ca[CB_{11}H_{12}]_2$·0.8H$_2$O, respectively. In comparison, $Zn[CB_{11}H_{12}]$·xH$_2$O was dried at 100 °C and 150 °C, with water content estimated to be approximately 3 mol, denoted as $Zn[CB_{11}H_{12}]_2$·3H$_2$O, and 2 mol, equally $Zn[CB_{11}H_{12}]_2$·2H$_2$O, respectively.

FTIR of the synthesised *closo*-monocarboranes determined that the cation exchange was successful for the hydrated Mg, Ca, and Zn compounds, with the loss of the C-H resonance at 3200 cm^{-1} from the precursor's Me_3NH^+ cation, along with the mode at 1450 cm^{-1} from the N-CH$_3$ bend (Figure S8). FTIR data sets for $Mg[CB_{11}H_{12}]_2$·3.1H$_2$O, $Ca[CB_{11}H_{12}]_2$·1.9H$_2$O, and $Zn[CB_{11}H_{12}]_2$·3H$_2$O show resonances at ~3600 - 3400 cm^{-1} (broad, O-H stretch) and 1600 cm^{-1} (H-O-H scissor) from water, which likely shows the presence of coordinated solvated water, but may also include water from the brief air exposure prior to FTIR measurements. The rapid hydration of the *closo*-monocarboranes is possible because all samples are deliquescent or hygroscopic, absorbing water quickly when exposed to air.[58] To attempt to clarify the presence of water in as-prepared samples, Raman spectroscopy was undertaken on powdered samples sealed in glass capillaries under argon (Figure S9). Raman showed that the divalent salts had no residual N-H resonances that would have indicated the presence of Me_3NH^+ at 3180 cm^{-1}. There was also a lack of C-H bands at 1457 cm^{-1} and 2967 cm^{-1} identified as resonances caused by the CH$_3$ groups of Me_3NH^+. The bands at 2572 cm^{-1} and from 947 – 575 cm^{-1} were attributed to the B-H of the *closo*-monocarborane anion, whereas the band at 3032 cm^{-1} was due to the C-H mode from the anion. However, it was still difficult to conclude the level of solvated water present in the samples as there was a very weak and broad band that appeared at ~3525 cm^{-1} indicating water in both $Mg[CB_{11}H_{12}]_2$·3.1H$_2$O and $Ca[CB_{11}H_{12}]_2$·1.9H$_2$O that was not observable in the sample for $Zn[CB_{11}H_{12}]_2$·3H$_2$O (Figure S9). The Raman signal from highly polar moieties, such as O-H, is often weak, unlike in FTIR. It is expected that the divalent salts still contain solvated water due to the high electron density of the divalent cations.[17]

A similar spectroscopic analysis was performed after the anhydrous synthesis of $Mg[CB_{11}H_{12}]_2$ and on its ethylenediamine analogue. FTIR of $Mg[CB_{11}H_{12}]_2$ indicated that the C-H stretch at 3200 cm^{-1} had significantly decreased in comparison to the B-H stretch of the cage at 2550 cm^{-1}, which indicated the loss of Me_3NH^+ (Figure S10). However, it was noted that there was some organic component (possibly hexane or dibutylmagnesium) remaining in the powder due to aliphatic C-H stretches at 2900 cm^{-1}, along with O-H stretches and bending resonances at ~3600 - 3400 cm^{-1} and ~1600 cm^{-1} that could be from brief air exposure (Figure S10). In comparison, minimal O-H stretches were seen in the FTIR for $Mg[CB_{11}H_{12}]_2$·3en but a doublet indicative of -NH$_2$ stretching resonances was present at 3300 - 3400 cm^{-1} with a -NH$_2$ bending resonance at 1570 cm^{-1}. Raman spectroscopy was attempted on both samples but was unable to be analysed due to severe fluorescence of the samples.

Powder X-ray diffraction (pXRD) was undertaken on samples: (a) $Me_3NH[CB_{11}H_{12}]$, (b) $Na[CB_{11}H_{12}]$, (c) $Zn[CB_{11}H_{12}]_2$·3H$_2$O, (d) $Mg[CB_{11}H_{12}]_2$·3.1H$_2$O, and (e) $Ca[CB_{11}H_{12}]_2$·1.9H$_2$O (Figure S11). The $Na[CB_{11}H_{12}]$ intermediate product used for the $M[CB_{11}H_{12}]_2$·xH$_2$O (*M* = Zn, Mg, Ca) synthesis was dried after reaction with NaOH and neutralised with HCl to compare its pXRD data with that of the final divalent products. The $Na[CB_{11}H_{12}]$ pXRD pattern matches the known orthorhombic structure available in the literature as well as a minor contamination of NaCl due to the neutralisation of excess NaOH with dilute HCl (Figure S11).[59] The subsequent XRD patterns for $Mg[CB_{11}H_{12}]_2$·3.1H$_2$O, $Zn[CB_{11}H_{12}]_2$·3H$_2$O and $Ca[CB_{11}H_{12}]_2$·1.9H$_2$O show no evidence of precursors such as: $MgCO_3$, $Mg(OH)_2$, $ZnCO_3$ and $CaCO_3$. $Ca[CB_{11}H_{12}]_2$·1.9H$_2$O has an amorphous or nano-crystalline structure as observed with a broad diffraction halo at 16° 2θ. A hydrated crystallographic structure has been published previously for $Mg(H_2O)_6[CB_{11}H_{12}]_2$·1.5H$_2$O from crystals grown from a slowly cooled saturated solution which was found to crystallise in a triclinic *P*1 space group.[13] However, as the $Mg[CB_{11}H_{12}]_2$·3.1H$_2$O sample analysed in this study was dried at 100 °C and estimated to only contain 3.1 mol coordinated water to 1 mol of $Mg[CB_{11}H_{12}]$ and thus does not match the known structure.

Synchrotron radiation X-ray diffraction (SR-XRD) was performed on $Mg[CB_{11}H_{12}]_2$ and $Mg[CB_{11}H_{12}]_2$·3en (Figure S12 and S13). $Mg[CB_{11}H_{12}]_2$ was indexed in hexagonal space group *R*3*c* (*a* = 10.39(1) Å, *c* = 21.33(2) Å, *V* = 1995(4) Å^3) but could not be structurally solved. $Mg[CB_{11}H_{12}]_2$·3en was indexed in orthorhombic *Pbca* (*a* = 14.73(1) Å, *b* = 21.87(2) Å, *c* = 19.06(2) Å, *V* = 6139(9) Å^3, *ρ* = 1.06 g/cm^3) and structurally solved using rigid bodies of $[CB_{11}H_{12}]^-$ anions and octahedrally coordinated

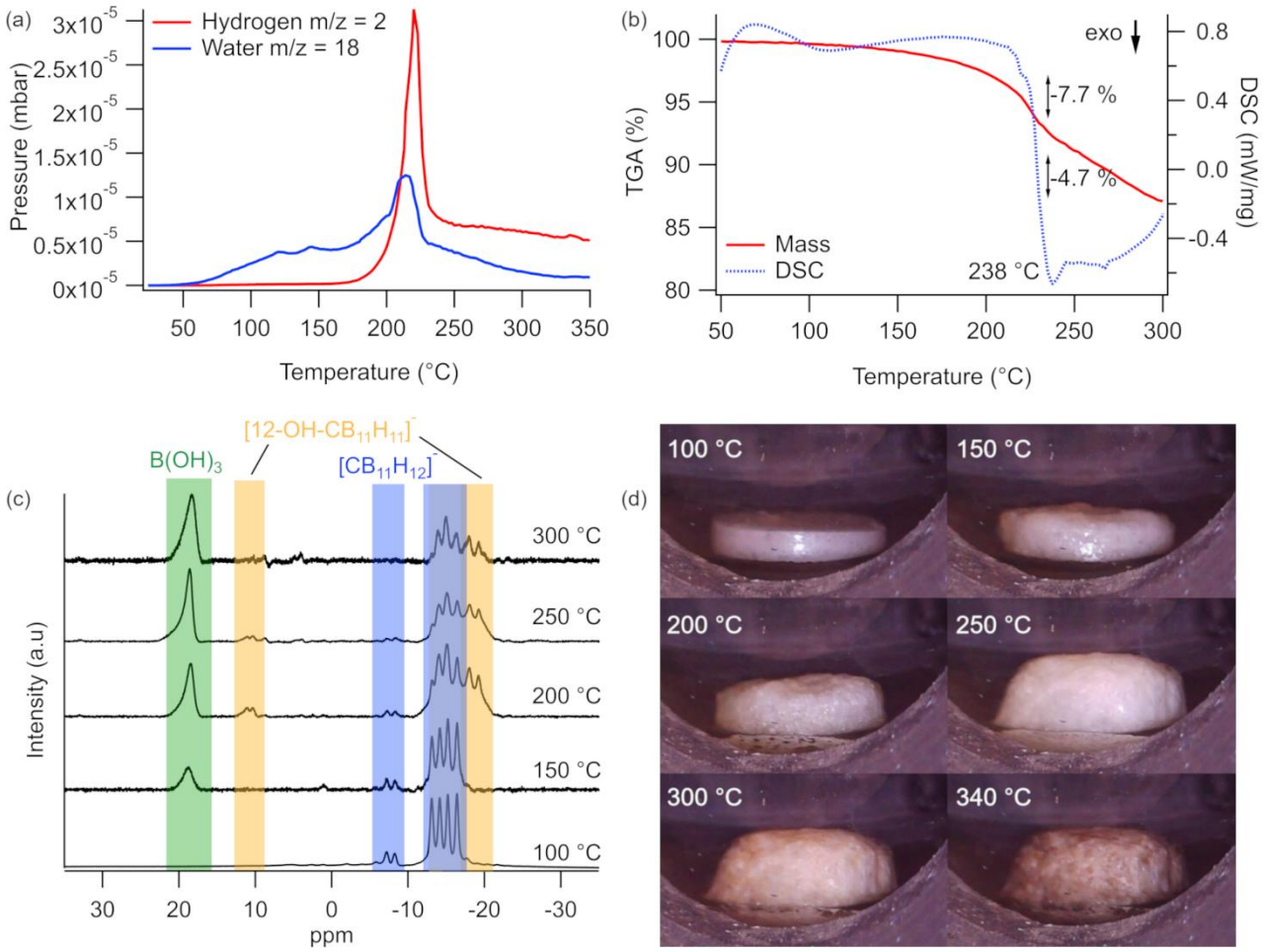

Figure 2 Thermal characteristics of $Mg[CB_{11}H_{12}]_2{\cdot}3.1H_2O$ according to (a) RGA-MS (vacuum, 10 °C/min), (b) DSC-TGA (40 mL/min Ar, 10 °C/min), (c) ^{11}B NMR in D_2O at room temperature for samples of $Mg[CB_{11}H_{12}]_2{\cdot}3.1H_2O$ previously heated under argon to the temperatures specified, and (d) TPPA of $Mg[CB_{11}H_{12}]_2{\cdot}3.1H_2O$ (4 °C/min, Ar atmosphere). For TPPA, the pellet diameter was 6 mm and the thickness at 24 °C was 1.01 mm. This thickness expanded to 1.91 mm at 340 °C.

$[Mg(en)_3]^{2+}$ clusters.[59,60] Atomic positions are provided in Table S2 and the structural coordination is shown in Figure 1.

Thermal properties

Thermal analysis of $Mg[CB_{11}H_{12}]_2{\cdot}3.1H_2O$ was undertaken using Differential Scanning Calorimetry - Thermogravimetric Analysis (DSC-TGA), Residual Gas Analysis - Mass Spectrometry (RGA-MS), *ex-situ* ^{11}B NMR, and Temperature programmable photographic analysis (TPPA) (Figure 2). Analysis of RGA-MS data indicated two minor water release events between 100 – 150 °C followed by a larger water release detected at 200 – 220 °C, coupled with a hydrogen release (Figure 2a). Comparatively, heating $Mg[CB_{11}H_{12}]_2{\cdot}3.1H_2O$ from 50 – 300 °C shows a mass loss of ~12 wt.% in TGA, beginning after 100 °C, commensurate with an exothermic peak at 220 °C in DSC (Figure 2b). The gradual mass loss above 100 °C indicates the stepwise loss of water due to the dehydration of the $Mg[CB_{11}H_{12}]_2{\cdot}3.1H_2O$ salt. However, at 220 °C, a sharp increase in hydrogen gas was detected along with a major mass loss event, indicating either decomposition of the $[CB_{11}H_{12}]^-$ cage, or hydrolysis of coordinated water before $Mg[CB_{11}H_{12}]_2{\cdot}3.1H_2O$ could be fully dehydrated. This is similar to what is observed in the thermal treatment of $[MgB_{12}H_{12}]{\cdot}xH_2O$ during attempted dehydration.[54,55] In the case of the $[B_{12}H_{12}]^{2-}$ anion, the formation of hydrogen bonds between Mg-coordinated water ($H^{\delta+}$) and the B-H ($H^{\delta-}$) units on the boron cage can result in hydroxylation.[54,55] A close proximity between coordinated water and B-H units, as water is released, increases the acidity of the protons on the coordinated water, resulting in the eventual hydroxylation of the boron cage (Scheme S1).[54,55] This has also been observed in $MgCl_2{\cdot}2H_2O$, where heating the solid salt under a constant stream of N_2 gas led to decomposition rather than dehydration.[61] In contrast, it is known that monohydroxylation of the $[CB_{11}H_{12}]^-$ anion is synthetically achievable by reacting $CsCB_{11}H_{12}$ with 80 % H_2SO_4 at 175 °C for 5 hours with a yield of 83 % for the $[12\text{-}HO\text{-}CB_{11}H_{11}]^-$ anion.[62] In an attempt to analyse $Mg[CB_{11}H_{12}]_2{\cdot}3.1H_2O$ during and after thermal treatment, a standard of $Na[12\text{-}HO\text{-}CB_{11}H_{11}]$ was synthesised separately to be used as a reference for monocarborane hydroxylation by ^{11}B NMR (Figure S14). Similar reactions have also been published to produce hydroxylated $[B_{12}H_{12-n}(OH)_n]^{2-}$ (n = 1-3) in less aggressive conditions, using 38 – 48 % H_2SO_4 and $Cs_2B_{12}H_{12}$ at 90 – 110 °C.[63] However, it must

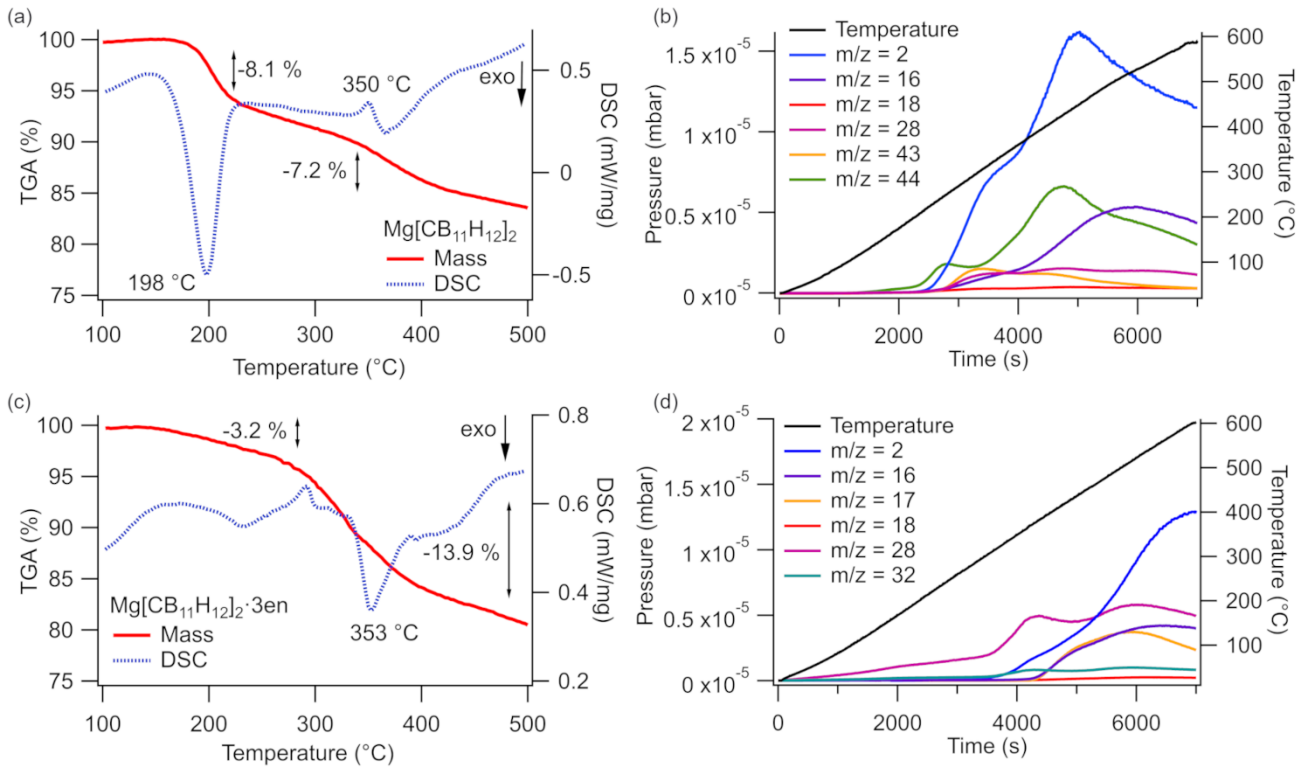

Figure 3 Thermal analysis of $Mg[CB_{11}H_{12}]_2$ and $Mg[CB_{11}H_{12}]_2{\cdot}3en$. (a) and (b) present the DSC-TGA and RGA-MS respectively for $Mg[CB_{11}H_{12}]_2$ synthesised via the reaction of excess $MgBu_2$ (1M, heptane) and $Me_3NH[CB_{11}H_{12}]$ in hexane. Likewise, the respective (c) DSC-TGA and (d) RGA-MS for $Mg[CB_{11}H_{12}]_2{\cdot}3en$ are shown. DSC-TGA was collected using and Ar flow of 40 mL/min with a 10 °C/min ramp rate. RGA-MS was performed under vacuum, with a heating rate of 10 °C/min.

be documented that the mono-hydroxylation of $[CB_{11}H_{12}]^-$ necessitates more acidic conditions compared to that of $[B_{12}H_{12}]^{2-}$, due to the less reactive nature of the *closo*-monocarbadodecaborate anion. Hydroxylation occurs at the boron opposite the carbon vertex due to the polarity of the cage, where the carbon vertex holds a more negative charge, decreasing electron density at the opposite vertex.[64] This is similar to the antipodal effect that causes a down field shift in ^{11}B NMR for the boron furthest from the carbon vertex.[65]

To identify the structural changes occurring when $Mg[CB_{11}H_{12}]_2{\cdot}3.1H_2O$ (dried at 100 °C) was heated, *ex-situ* room temperature ^{11}B NMR (D_2O) analysis was performed on $Mg[CB_{11}H_{12}]_2{\cdot}3.1H_2O$ salts dried at different temperatures (150, 220, 280, and 350 °C) under constant argon flow (Figure 2c). As the drying temperature was increased, the $[CB_{11}H_{12}]^-$ doublets at -7.5, -13.5, and -16.0 ppm all decrease in intensity, with increased intensity of a doublet at -19 ppm. The -19 ppm resonance matches that of the previously discussed hydroxylated $[12\text{-HO-}CB_{11}H_{11}]^-$ anion (Figure S14) with ^{11}B NMR chemical shifts ($Na[12\text{-OH-}CB_{11}H_{11}]$ in CD_3CN) at +11.06 ppm (singlet, 1B), -16.82 ppm (doublet, 5B), and -19.10 ppm (doublet, 5B). It is possible to see the hydroxylated anion in ^{11}B NMR of the $Mg[CB_{11}H_{12}]_2{\cdot}3.1H_2O$ samples dried at high temperature, particularly at 280 °C (Figure 2c). However, it should also be noted that there was a significant amount of powder in these high temperature dried samples (above 200 °C) that did not dissolve in D_2O or CD_3CN. In particular, an absence of resonances for the sample heated to 350 °C (not shown) could be due to the total formation of water-insoluble products. The DSC-TGA, RGA-MS, and ^{11}B NMR results indicated that $Mg[CB_{11}H_{12}]_2{\cdot}3.1H_2O$ could in fact be less stable than $Mg(H_2O)_6[B_{12}H_{12}]_2$ when thermally treated. TGA data on $Mg(H_2O)_6[B_{12}H_{12}]_2$ by Shore *et. al*,[55] showed that heating (10 °C/min, 40 mL/min Ar) $Mg(H_2O)_6[B_{12}H_{12}]_2$ leads to the stepwise dehydration of 3 waters to $Mg(H_2O)_3[B_{12}H_{12}]_2$ at 200 °C, followed by hydrogen loss at $T > 250$ °C with the formation of the polyhydroxylated compound, $Mg(\mu\text{-}OH)_x[B_{12}H_{12-x}]_2$. Whereas, we see the hydroxylation of $Mg[CB_{11}H_{12}]_2{\cdot}3.1H_2O$ already occurring at 200 °C in ^{11}B NMR and a large hydrogen release before 250 °C in RGA-MS.

TPPA of $Mg[CB_{11}H_{12}]_2{\cdot}3.1H_2O$ visualises the dehydration and decomposition of the pelletised salt as it was heated under Ar (Figure 2d). Little physical change was observed up to 100 °C, however at 150 °C, the pellet becomes at least partially molten, indicated by bubbling on the surface of the pellet as dehydration of the sample occurs. Between 200 – 250 °C, the pellet expands to a froth-like morphology, which was approximately two times its original height, followed by a change in colour from white to brown, possibly due to the formation of decomposition products such as elemental boron, or other magnesium borates/borides.

Initial DSC-TGA and RGA-MS results indicated a definite difference in the decomposition processes of both $Mg[CB_{11}H_{12}]_2$ and $Mg[CB_{11}H_{12}]_2{\cdot}3en$ in contrast to $Mg[CB_{11}H_{12}]_2{\cdot}3.1H_2O$ (Figure 3). Firstly, $Mg[CB_{11}H_{12}]_2$ underwent an initial mass loss

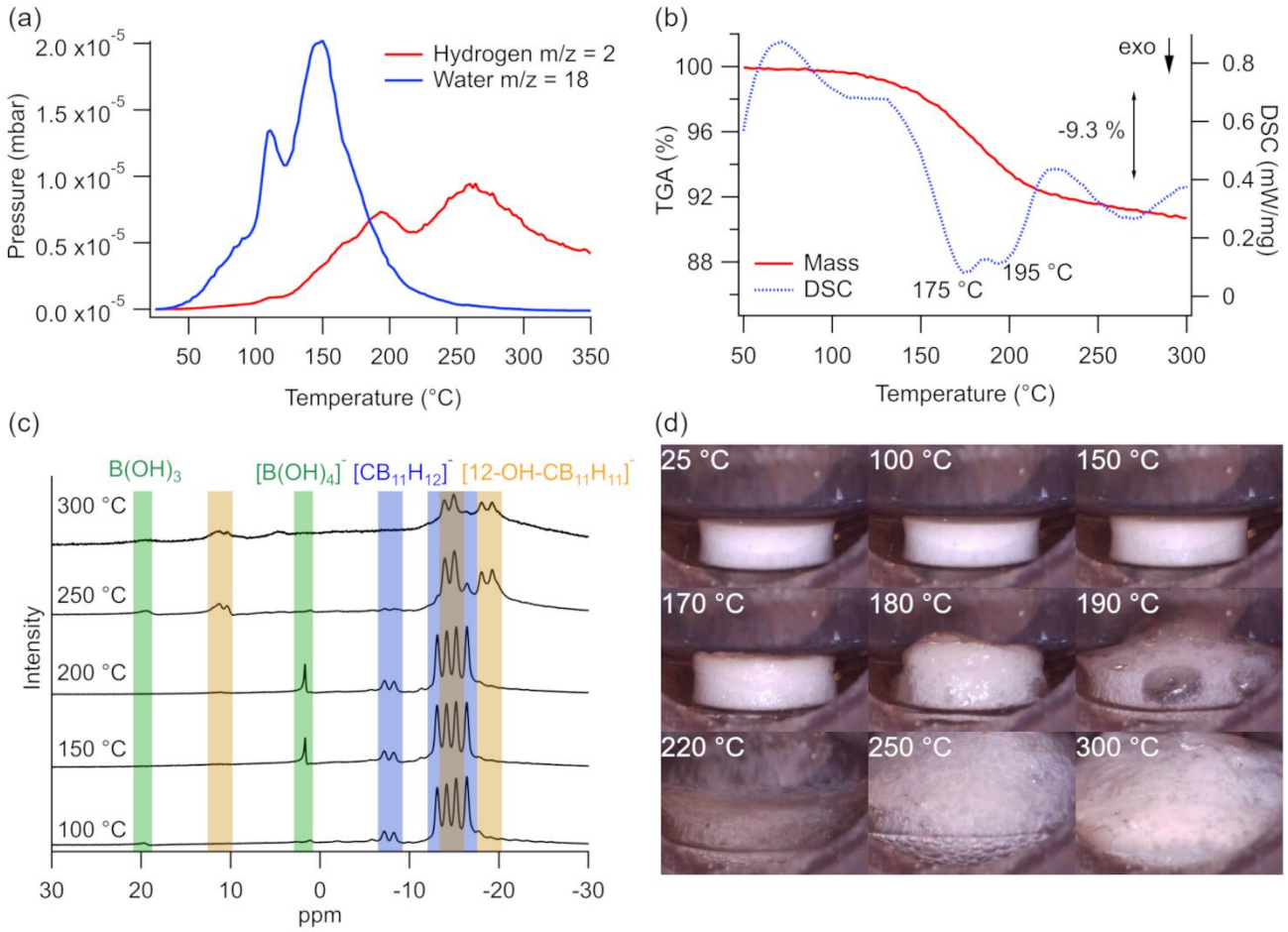

Figure 4 Thermal characteristics of $Ca[CB_{11}H_{12}]_2{\cdot}xH_2O$ according to (a) RGA-MS (vacuum, 10 °C/min), (b) DSC-TGA (40 mL/min Ar, 10 °C/min), (c) ^{11}B NMR in D_2O at room temperature of samples of $Ca[CB_{11}H_{12}]_2{\cdot}xH_2O$ heated under argon to the temperatures specified, and (d) TPPA of $Ca[CB_{11}H_{12}]_2{\cdot}xH_2O$ (4 °C/min, Ar atmosphere). Key compounds are highlighted in green ($B(OH)_3$/$B(OH)_4^-$), blue ($[CB_{11}H_{12}]^-$), and yellow ($[12\text{-}OH\text{-}CB_{11}H_{11}]^-$) in ^{11}B NMR. For TPPA, the pellet diameter was 6 mm and the thickness was 1.92 mm.

at 200 °C of 8.1 wt.%, which coincides with an exothermic peak in DSC, followed by a second mass loss between 300 – 400 °C of 7.2 wt.% associated with an endo- and exothermic peak (Figure 3a). However, pristine $Mg[CB_{11}H_{12}]_2$ should only have a hydrogen content of only 7.79 wt.%, thus, the mass loss must also result from the loss of another compound or impurity. Previously, it was mentioned that a residual amount of trimethylamine (NMe_3 or Me_2NH) was detected by ^1H NMR in the prepared $Mg[CB_{11}H_{12}]_2$ that was present due to the deprotonation of the Me_3NH^+ cation during synthesis even after dying the powder at 100 °C. However, after heating the as-prepared $Mg[CB_{11}H_{12}]_2$ under vacuum at 215 °C, an impurity was still observed in ^1H NMR (Figure S15), with a slightly broadened, less intense resonance at 2.15 ppm. The RGA-MS collected during thermal treatment of $Mg[CB_{11}H_{12}]_2$ indicated that there were multiple gas release events, with the first at ~200 °C showing peaks with an *m/z* of 2, 28, 43, and 44; however, it was difficult to identify this species but is likely due to the decomposition of an alkane species, possibly $MgBu_2$ (Figure 3b). A further mass loss was detected above 350 °C due to decomposition of the material with *m/z* = 44, 16, and 2 (Figure 3b and S15). This may be due to the decomposition of the unidentified coordinated species seen in ^1H NMR as well as the boron cage. Theoretically, the *m/z* peak at 44 could indicate the presence of dimethylamine, which would agree with the resonance at 2.10 ppm in ^1H NMR (Figure S2). The thermal analysis results indicate that $Mg[CB_{11}H_{12}]_2$ is not solvent-free as expected, likely due to its strongly coordinating cation.

$Mg[CB_{11}H_{12}]_2{\cdot}3en$ showed a gradual loss of mass up to 300 °C, which overlaps with a broad exotherm in DSC-TGA (Figure 3c). This was followed by a significant mass loss that was indicative of decomposition of the $Mg[CB_{11}H_{12}]_2{\cdot}3en$. RGA-MS shows multiple overlapping gas release events showing the decomposition of $Mg[CB_{11}H_{12}]_2{\cdot}3en$, however, *m/z* = 30, the base peak for ethylenediamine was not observed. Nevertheless, it was observed that *m/z* = 28, 17 and 16 which are typical base peaks for ethane, ammonia and methane (C_2H_6, NH_3 and CH_4) were visible, indicating that decomposition of ethylenediamine, rather than desolvation, occurred above temperatures of 350 °C. Coupled with the results from *in situ* SR-XRD of $Mg[CB_{11}H_{12}]_2{\cdot}3en$ (Figure S16) that show a loss of crystallinity at 250 °C, it can be inferred that full decomposition occurs above this temperature.

Thermal characteristics of $Ca[CB_{11}H_{12}]_2{\cdot}1.9H_2O$ pre-dried at 100 °C were investigated using DSC-TGA, RGA-MS, TPPA and *ex-situ* ^{11}B NMR. A 9.3 wt.% mass loss from $Ca[CB_{11}H_{12}]_2{\cdot}1.9H_2O$ was

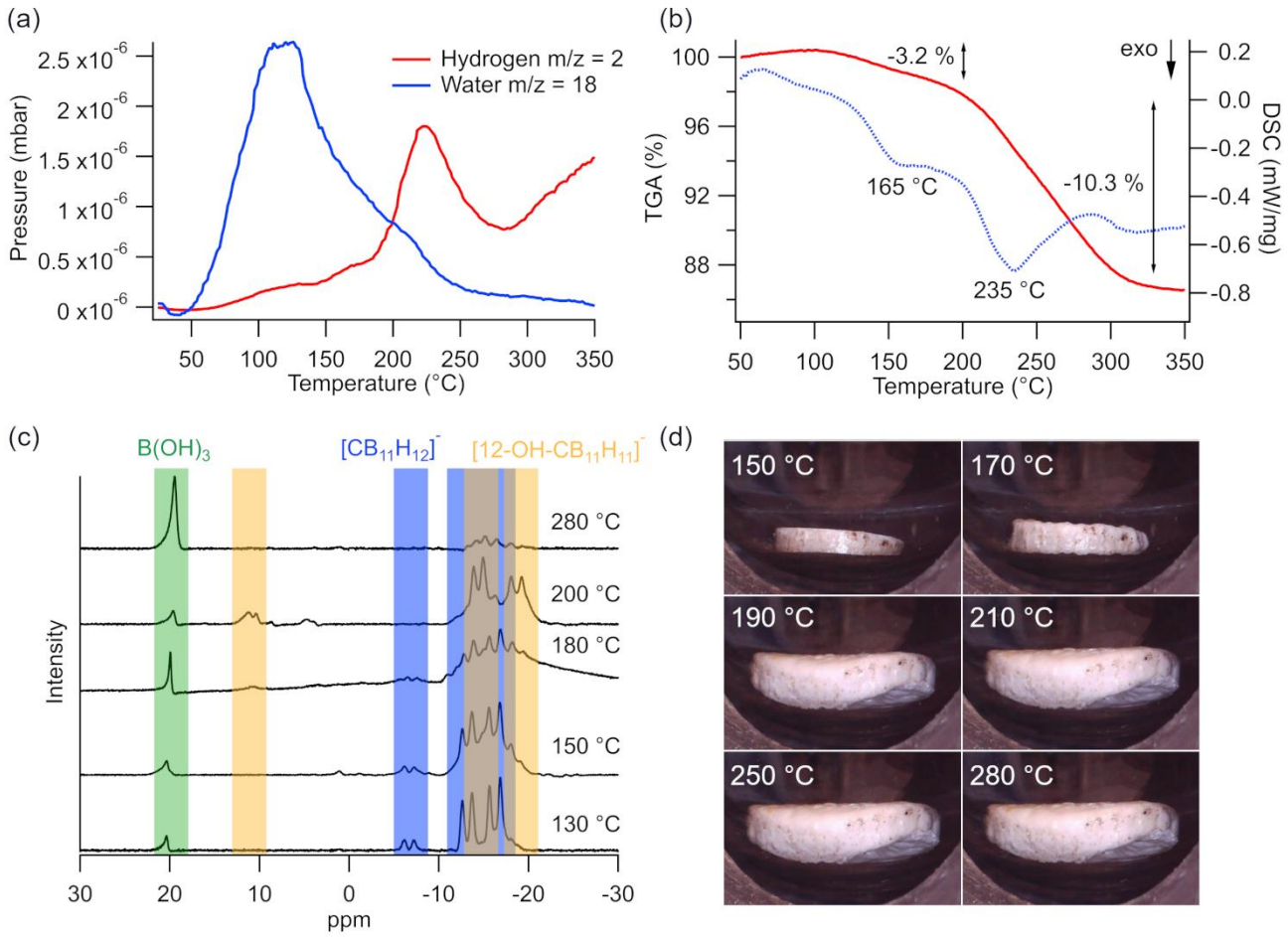

Figure 5 Thermal characteristics of $Zn[CB_{11}H_{12}]_2{\cdot}xH_2O$ according to (a) RGA-MS (Vacuum, 10 °C/min), (b) DSC-TGA (bottom) (40 mL/min Ar, 10 °C/min, 4.67 mg), (c) ^{11}B NMR in D_2O at room temperature of samples of $Zn[CB_{11}H_{12}]_2{\cdot}xH_2O$ heated under argon to the temperatures specified, and (d) TPPA of $Zn[CB_{11}H_{12}]_2{\cdot}xH_2O$ (4 °C/min, Ar atmosphere). Key compounds are highlighted in green ($B(OH)_3$), blue ($[CB_{11}H_{12}]^-$), and yellow ($[12\text{-}OH\text{-}CB_{11}H_{11}]^-$). For TPPA, the initial pellet diameter was 6 mm and the thickness was 1.00 mm.

detected between 100 – 300 °C by TGA, which, in addition to RGA-MS, indicated that this is primarily due to the loss of water (Figure 4a and 4b). The dehydration occurred in a stepwise fashion, as indicated by the two peaks in water vapour pressure at 110 °C and 150 °C. There is also a slight overlap between the release of water and the onset of H_2 release near 150 °C as detected by RGA-MS (Figure 4a). The hydrogen pressure shows a gradual increase from 125 °C, with broad peaks detected at ~200 °C and 270 °C, indicative of decomposition. DSC showed overlapping exothermic peaks at 175 and 195 °C, and a third broad peak at 260 °C, which appear to be correlated with decomposition and hydrogen release (Figure 4b). Therefore, The decomposition of $Ca[CB_{11}H_{12}]_2{\cdot}1.9H_2O$ proceeds in a different manner to $Mg[CB_{11}H_{12}]_2{\cdot}3.1H_2O$, with dehydration before decomposition.

TPPA of $Ca[CB_{11}H_{12}]_2{\cdot}1.9H_2O$ visually indicated that little change was visible in the pelletised sample up to 150 °C under argon (Figure 4d). However, at 170 °C, gas was released as shown by the bubbling on the surface of the pellet from a liquid-like layer before complete melting by 190 °C. The melting of other solvated metal boranes is known to occur, for example, powders of $Li_2B_{12}H_{12}$ coordinated with acetonitrile melt at 150 °C.[66] The $Ca[CB_{11}H_{12}]_2{\cdot}1.9H_2O$ remained a liquid until 230 – 250 °C, where the sample began to solidify due to decomposition commensurate with the loss of water and/or hydrogen. This decomposition temperature is in agreement with what was observed in the RGA-MS, where only hydrogen is detected at T > 250 °C without any water vapour. TPPA showed the sample forming an expansive white frothy solid from 250 °C. ^{11}B NMR was conducted after heating the sample to a selection of different temperatures to identify the decomposition pathway for hydrated $Ca[CB_{11}H_{12}]_2{\cdot}1.9H_2O$ (Figure 4c). In comparison to $Mg[CB_{11}H_{12}]_2{\cdot}xH_2O$, when preparing the samples in D_2O for analysis, the sample fully dissolved, indicating the solubility of all products after heating to the temperatures analysed. While the hydrated calcium salt seems to be stable in molten form up to 250 °C, it is obvious that the hydroxylation of the carborane cage occurs after this temperature (Figure 4c), coinciding with the loss of hydrogen at elevated temperatures (Figure 4a). Despite the fact that DSC-TGA and RGA-MS suggests there is no more water release from the calcium salt above 250 °C it is possible that the $Ca[CB_{11}H_{12}]_2{\cdot}1.9H_2O$ contains strongly

coordinated water due to the fact that the hydroxylated carborane anion [12-OH-$CB_{11}H_{11}$]$^-$ could be observed to form at 250 °C by ^{11}B NMR. This hydroxylation indicated water remains present to enable this reaction to occur (Figure 4c).

Recently, anhydrous $Ca[CB_{11}H_{12}]_2$ was reported to be synthesised in a similar fashion to the present study, via the neutralisation of $[H_3O][CB_{11}H_{12}]$ with $CaCO_3$ and removal of water under vacuum at 160 °C for 10 hours.[14] According to Raman spectroscopy and ^{1}H NMR, the material was deemed anhydrous.[14] These results are in contrast to the results observed herein, indicating that isothermal conditions for dehydration may be beneficial. However, the presence of hydrogen release in the present RGA-MS data below 150 °C does indicate that partial decomposition could occur under these conditions. In the analogous $[B_{12}H_{12}]^{2-}$ system, $[Ca(H_2O)_7][B_{12}H_{12}]\cdot H_2O$ can be dehydrated at 300 °C to form anhydrous $CaB_{12}H_{12}$.[14,67] The greater stability of the $[B_{12}H_{12}]^{2-}$ compound compared to the $[CB_{11}H_{12}]^-$ when coordinated to Ca^{2+} is similar to results for Mg^{2+}, indicating that the hydrated carborane salts are less thermally stable than the decaborane salts when they are hydrated. It is also apparent that the calcium *closo*-monocarborane salt is more stable than the magnesium salt from the elevated hydroxylation temperatures seen by *ex situ* ^{11}B NMR. This is expected as the charge density of magnesium is significantly higher than for calcium, therefore, it has a higher affinity towards coordinating to solvents such as water and CH_3OH.[17,54]

DSC-TGA and RGA-MS (Figure 5a and 5b) for hydrated $Zn[CB_{11}H_{12}]_2\cdot 3H_2O$ (dried at 100 °C) shows a decrease in mass of 3 wt.% up to 150 °C that coincides with the loss of water. This event is followed by the loss of hydrogen, but the large mass loss of 10 wt.% in TGA suggests that additional water may also be lost at higher temperatures under argon (DSC-TGA) compared to vacuum (RGA-MS). It appears there is significant dehydrogenation and eventual decomposition of the $[CB_{11}H_{12}]^-$ cage above 200 °C. The hydrogen release could also indicate that, similar to the Mg and Ca salts, the dehydration of the Zn salt may result in similar hydroxylated products. Analysis of *ex-situ* ^{11}B NMR showed this to be true with the identification of [12-OH-$CB_{11}H_{11}$]$^-$ being formed above 150 °C (Figure 5c), at a lower temperature than both the Mg and Ca analogues. The $[CB_{11}H_{12}]^-$ anion was almost completely converted to the hydroxylated anion by 200 °C. Again, similar to what was observed with the hydrated $Mg[CB_{11}H_{12}]_2\cdot 3.1H_2O$ salt, the [12-OH-$CB_{11}H_{11}$]$^-$ anion then decomposed into products that were indistinguishable by ^{11}B NMR (Figure 5c). It should be noted that there were also significant amounts of white solid that did not dissolve in D_2O for the thermally treated material.

TPPA of $Zn[CB_{11}H_{12}]_2\cdot 3H_2O$ is also interesting as, comparable to $Mg[CB_{11}H_{12}]_2\cdot 3.1H_2O$, the pellet of $Zn[CB_{11}H_{12}]_2\cdot 3H_2O$ expanded in size significantly at T > 150 °C from a diameter of 6.0 mm to 8.9 mm (increase of 33 %) and a thickness of 1.0 mm to 1.6 mm (increase of 38 %) (Figure 5d). Unlike $Ca[CB_{11}H_{12}]_2\cdot<3H_2O$, no melting is seen in the TPPA for $Zn[CB_{11}H_{12}]_2\cdot 3H_2O$ (Figure 5d). The similarities between the thermal analysis of the zinc and magnesium salts was significant, and could be related to the similarity between the cations. Both hexacoordinated Zn^{2+} and

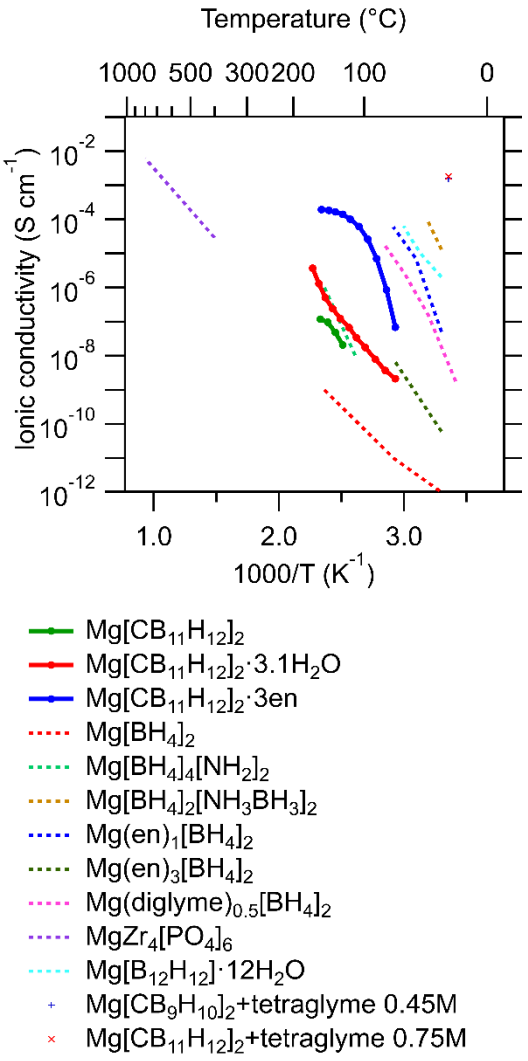

Figure 6 Ionic conductivity measured using electrochemical impedance spectroscopy (EIS) of $Mg[CB_{11}H_{12}]_2\cdot 3.1H_2O$, $Mg[CB_{11}H_{12}]_2$ and $Mg[CB_{11}H_{12}]_2\cdot 3en$ compared to other magnesium solid-state electrolytes.[20,23,25–27,60,69–71]

Mg^{2+} have similar ionic radii of 74 pm and 72 pm, respectively, whereas, Ca^{2+} is significantly larger at 100 pm (coordination number = 6).[68] The charge density of Zn^{2+} is also similar to that of Mg^{2+}, thus, it would be expected that thermal dehydrogenation and decomposition would proceed in similar processes when heated to high temperatures.[17]

Ionic conductivity and electrochemical stability

The ionic conductivity of the solid-state divalent *closo*-monocarboranes was measured as a function of temperature using electrochemical impedance spectroscopy (EIS) (Figure 6a, 7a and 8). $Mg[CB_{11}H_{12}]_2\cdot 3.1H_2O$ displayed ionic conductivity of 2×10^{-9} S cm^{-1} at 70 °C, and 3×10^{-6} at 170 °C (Figure 6). This was higher than many previously reported ionic conductivities for other Mg solid-state electrolytes, including $Mg[BH_4]_2$ and $MgZr_4(PO_4)_6$.[20,23,25–27,60,69–71] Comparatively, solvent-free $Mg[CB_{11}H_{12}]_2$ had lower ionic conductivity than the hydrated $Mg[CB_{11}H_{12}]_2\cdot 3.1H_2O$, which showed similarities to the trends seen for $Mg[BH_4]_2$ and its solvated counterparts (Figure 6).[70] To

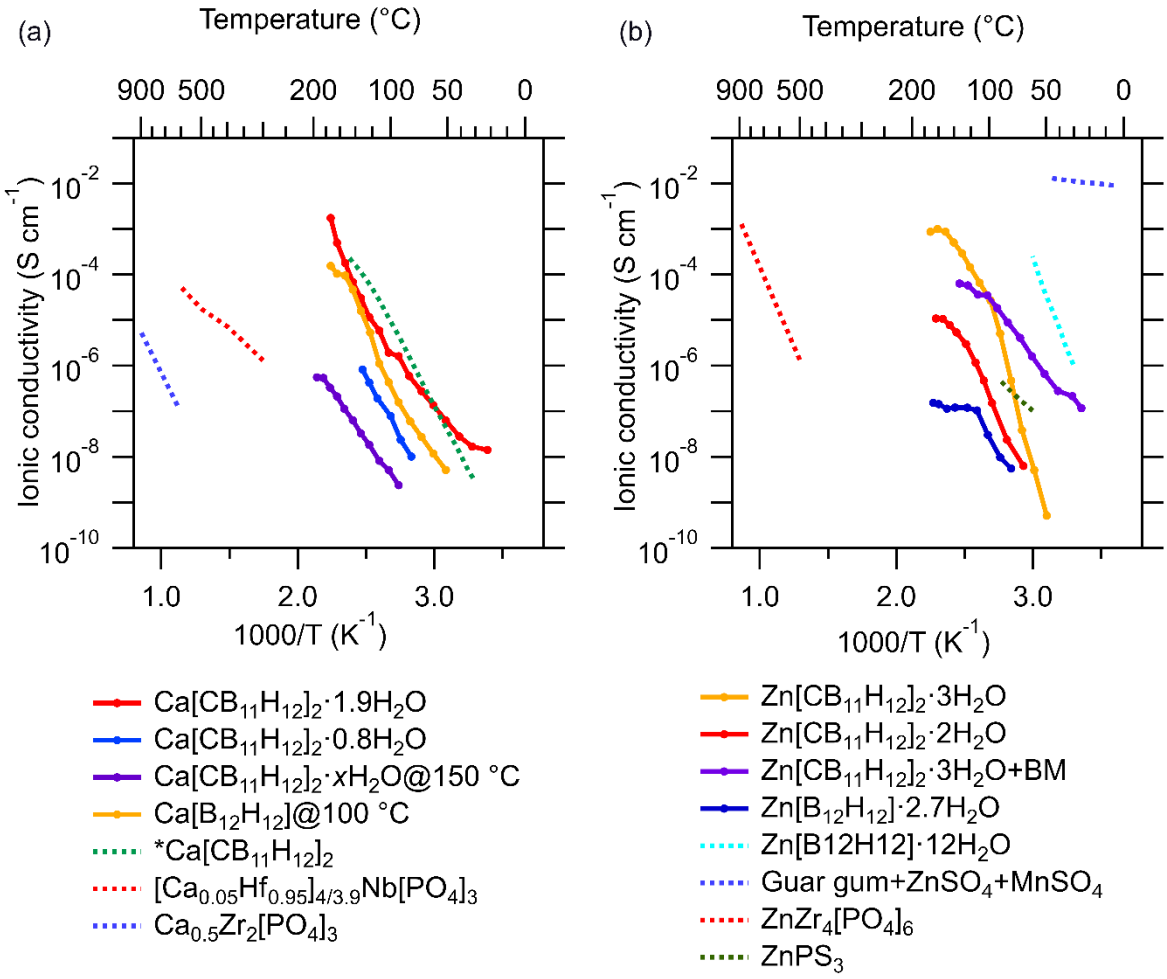

Figure 7 Ionic conductivity determined using EIS (a) of $Ca[CB_{11}H_{12}]_2{\cdot}xH_2O$ dried at 100, 125, and 150 °C, and (b) $Zn[CB_{11}H_{12}]_2{\cdot}xH_2O$ dried at 100 °C, 150 °, and dried at 150 °C and ball milled 1 hour (0.6 mm stainless steel balls, 33:1 ball to sample mass ratio, 20 min each direction). (a) includes a comparison of the ionic conductivity of ceramic calcium electrolytes, $[Ca_{0.05}Hf_{0.95}]_{4/3.9}Nb[PO_4]_3$, $Ca_{0.5}Zr_2[PO_4]_3$, and $Ca[CB_{11}H_{12}]_2$ synthesised by Kisu et. al.[14,28,29] In (b) $Zn[B_{12}H_{12}]{\cdot}xH_2O$ dried at 100 °C has also been synthesised for comparison as well as solid-state electrolytes are also shown for comparison, including $ZnZr_4(PO_4)_6$, $ZnPS_3$, and aqueous polymer 'psuedo' solid electrolyte of $ZnSO_4$ in guar gum.[30,31,33]

assess the ionic conductivity of solvated Mg^{2+} in the $Mg[CB_{11}H_{12}]_2$ system, $Mg[CB_{11}H_{12}]_2{\cdot}3en$ was synthesised as ethylenediamine has been previously shown to be beneficial in improving ionic conductivity in other systems.[26] When ionic conductivity was analysed, $Mg[CB_{11}H_{12}]_2{\cdot}3en$ was found to have a higher conductivity at 70 °C of 6.8×10^{-8} S cm^{-1} compared to 2.1×10^{-9} S cm^{-1} at the same temperature for $Mg[CB_{11}H_{12}]_2{\cdot}3.1H_2O$. The ionic conductivity at 150 °C of $Mg[CB_{11}H_{12}]_2{\cdot}3en$ was also significantly higher than $Mg[CB_{11}H_{12}]_2{\cdot}3.1H_2O$ with conductivities of 1.9×10^{-4} S cm^{-1} as opposed to 5×10^{-7} S cm^{-1}, respectively. Similar increases in ionic conductivity have also been observed for solvated $Mg[BH_4]_2$.[26,69,70] In comparison to pure γ-$Mg[BH_4]_2$, which has an ionic conductivity of 5.3×10^{-14} S cm^{-1} at 40 °C, complexation of solvents including diglyme or ethylenediamine (en) have been shown to improve the ionic conductivity at 80 °C for $Mg(diglyme)_{0.5}[BH_4]_2$ and $Mg(en)[BH_4]_4$ to 2×10^{-5} S cm^{-1} and 6×10^{-5} S cm^{-1}, respectively (Figure 6a).[26,69,70]

Stability of the electrolytes against an Mg anode must be analysed to determine the suitability of these compounds for battery applications as solvates may be more prone to oxidising the metallic anode. Linear sweep voltammetry (LSV) of pellets of $Mg[CB_{11}H_{12}]_2{\cdot}3.1H_2O$, $Mg[CB_{11}H_{12}]_2$, and $Mg[CB_{11}H_{12}]_2{\cdot}3en$ against metallic Mg are shown in Figure S17a-c and was performed in the method described by Asakura *et al.*[72] A comparison of the three solid-state electrolytes indicated that $Mg[CB_{11}H_{12}]_2{\cdot}3.1H_2O$ had the highest oxidative stability of 1.9 V (Mg^{2+}/Mg), contrasted to 1.25 V and < 1 V for $Mg[CB_{11}H_{12}]_2$ and $Mg[CB_{11}H_{12}]_2{\cdot}3en$, respectively. The reasoning for the low oxidative stability of $Mg[CB_{11}H_{12}]_2$ could possibly be attributed to its impurity that had previously been discussed (Figure S5). However, it was also surprising to see that the oxidative stability of $Mg[CB_{11}H_{12}]_2{\cdot}3en$ was so low compared to $Mg[CB_{11}H_{12}]_2{\cdot}3.1H_2O$. It can be concluded that ethylenediamine is less stable than water as a solvate against oxidation at the Mg anode. There is minimal information on the oxidative stability of ethylenediamine as a ligand for borohydride based solid electrolytes. However, previous studies investigating the electrochemical stability of $Mg(en)[BH_4]_2$, found that irreversible oxidation occurred at voltages greater than 1.2 V at 60 °C using cyclic voltammetry (CV), indicating that electrochemical stability is limited.[26] Nonetheless, this

difference could be due to the decreased number of coordinated solvent molecules to Mg^{2+} or lower scan rates used (10 mV/s).[26]

The ionic conductivity of $Ca[CB_{11}H_{12}]_2{\cdot}1.9H_2O$ is displayed in Figure 7a along with other solid-state Ca^{2+} ionic conductors. The ionic conductivity was measured on multiple samples of $Ca[CB_{11}H_{12}]_2{\cdot}xH_2O$ dried at 100 °C, 125 °C, and 150 °C in order to analyse the effect of partial dehydration (Figure 7a). For $Ca[CB_{11}H_{12}]_2{\cdot}1.9H_2O$ dried at 100 °C, the ionic conductivity was significantly higher than for all other samples pre-dried at higher temperatures, with an ionic conductivity of 1×10^{-8} S cm^{-1} at 20 °C. In comparison to $Mg[CB_{11}H_{12}]_2{\cdot}3en$, $Ca[CB_{11}H_{12}]_2{\cdot}1.9H_2O$ showed similar ionic conductivities at 150 °C, for example 1.8×10^{-4} S cm^{-1} for $Mg[CB_{11}H_{12}]_2{\cdot}3en$ and 1.6×10^{-4} S cm^{-1} for $Ca[CB_{11}H_{12}]_2{\cdot}1.9H_2O$. The sample dried at 100 °C also showed excellent ionic conductivity up to 170 °C (1.7×10^{-3} S cm^{-1}). After this temperature, ionic conductivity was not able to be measured due to the melting as seen in TPPA (Figure 4b), and the subsequent short-circuit of the cell. The decrease in ionic conductivity in $Ca[CB_{11}H_{12}]_2{\cdot}xH_2O$ as it is dehydrated demonstrates the importance of the solvate in the process of ionic conduction in the solid-state. It has been shown that the solvation of other metal boron-based salts can lead to elevated ionic conductivities, which could open up a wealth of research opportunities in understanding the mechanism and benefit of various candidates.[18,23,25,26,70]. The beneficial effect of coordinated water increasing ionic conductivity was not surprising, as water has been found to increase the cationic conductivity in the solid electrolyte $Li_2Sn_2S_5$ as well as layered silicate compounds.[73] The presence of water was also recently proven to enhance the ionic conductivity of the *nido*-borane salts, $LiB_{11}H_{14}{\cdot}nH_2O$ and $NaB_{11}H_{14}{\cdot}nH_2O$.[18] In particular, for $NaB_{11}H_{14}$, the coordination of water was preferred compared to diglyme (diglycol methyl ether), with an ionic conductivity at 25 °C of 1.1×10^{-3} S cm^{-1} for $NaB_{11}H_{14}{\cdot}(H_2O)_n$ compared to 1.1×10^{-6} S cm^{-1} for $NaB_{11}H_{14}{\cdot}(\text{diglyme})_n$.[18]

If calcium *closo*-monocarborane was to be used as a solid-state electrolyte in a calcium battery, then it is important to understand its electrochemical stability against the metal. The oxidative stability of $Ca[CB_{11}H_{12}]_2{\cdot}1.9H_2O$ (dried at 100 °C) against a Ca metal anode was analysed using linear sweep voltammetry (LSV) (Figure S18), which has been used to study a number of metal-boron-hydrogen solid-state ionic conductors.[18] Using a scan rate of 50 μV s^{-1} and 100 °C, the oxidative stability was shown to be 3.03 V vs Ca^{2+}/Ca with smaller contributions at 2.4 V vs Ca^{2+}/Ca. The low electrochemical stability of $Ca[CB_{11}H_{12}]_2{\cdot}1.9H_2O$ against Ca metal and $Mg[CB_{11}H_{12}]_2{\cdot}3.1H_2O$ against Mg metal was attributed to the high reactivity of metals with water. In particular, pure Ca metal is well known to be highly reactive in water forming $Ca(OH)_2$ and H_2 in a highly exothermic reaction. Mg metal anodes have also been proven to be highly susceptible to the formation of impermeable $Mg(OH)_2$ interphases due to side reactions with water.[74]

$Zn[CB_{11}H_{12}]_2{\cdot}3H_2O$ showed higher ionic conductivity in the sample dried at 100 °C compared to that dried at 150 °C (Figure 7b), in a similar way to $Ca[CB_{11}H_{12}]_2{\cdot}xH_2O$. Similarly, this can be attributed to the greater presence of crystalline water, which may aid the mobility of the cation through the solid electrolyte. At $T > 150$ °C, the ionic conductivity of $Zn[CB_{11}H_{12}]_2{\cdot}xH_2O$ (dried at both 100 and 150 °C) decreased. This could be attributed to the decomposition and hydroxylation as seen in Figure 5c.

An attempt to increase ionic conductivity of $Zn[CB_{11}H_{12}]_2{\cdot}xH_2O$ by ball milling was undertaken for the powder (dried at 100 °C) for 1 hour (Figure 7b). Mechanically milling is believed to increase defects in the crystal structure, thus providing more pathways for ionic migration.[75] This has been previously shown to increase ionic conductivity In $Na[CB_{11}H_{12}]$ by stabilising the highly conductive bcc structure.[75] Mechanical milling can also create amorphous phases, for example, amorphous $Mg(BH_4)_2$ had a higher ionic conductivity compared to γ-$Mg(BH_4)_2$.[69] After milling $Zn[CB_{11}H_{12}]_2{\cdot}xH_2O$, a dramatic increase in ionic conductivity was observed at low temperatures (< 100 °C) (1.17×10^{-7} S cm^{-1} at 25 °C). Whereas pristine $Zn[CB_{11}H_{12}]_2{\cdot}3H_2O$ had an ionic conductivity ~1×10^{-10} S cm^{-1} at 50 °C. Previously, mixtures of $Na[CB_{11}H_{12}]$ and $Na_2[B_{12}H_{12}]$ were shown to increase the room temperature ionic conductivity.[45,48] Thus, further efforts to increase the ionic conductivity of Zn *closo*-monocarborane were attempted by forming ball milled mixtures of $Zn[CB_{11}H_{12}]_2{\cdot}xH_2O$ and $ZnB_{12}H_{12}{\cdot}xH_2O$ in 0.7:0.3, 0.5:0.5, and 0.3:0.7 molar ratios (Figure S19). However, this did not show any improvement in ionic conductivity compared to that of ball milled $Zn[CB_{11}H_{12}]_2{\cdot}xH_2O$ (Figure S19).

From Figures 7a and b, it is observed that ionic conductivities of Ca and Zn salts of $[CB_{11}H_{12}]^-$ are higher than those of their $[B_{12}H_{12}]^{2-}$ analogues. This can be potentially explained by the greater negative charge of the $[B_{12}H_{12}]^{2-}$ anion compared to the monovalent $[CB_{11}H_{12}]^-$ anion, thus cations would have higher electrostatic attraction to the $[B_{12}H_{12}]^{2-}$ anion. The anionic charge density is not a true measure of ionic conductivity, however, as has been shown for large $Na_2[B_{12}X_{12}]^{2-}$ (X = Cl, Br, I) compounds, where their anisotropic electron density was also a key factor in cation-anion bonding.[76] The addition of carbon into the anion lowers its charge, but also decreases the symmetry of the anion, and creates a dipole that lowers the activation energy for rotation.[44] This was found to be potentially significant for the increase in ionic conductivity for $Na[CB_{11}H_{12}]$ compared to $Na_2[B_{12}H_{12}]$ which have ionic conductivities of 10^{-5} S cm^{-1} at 25 °C and 10^{-7} S cm^{-1} at 50 °C, respectively.[44,59,77] While the solid-state ionic conductivity of $Zn[CB_{11}H_{12}]_2{\cdot}xH_2O$ is not particularly remarkable, compared to other solid-state ionic conductors, including $ZnZr_4[PO_4]_2$ and $ZnPS_3$, ball milled $Zn[CB_{11}H_{12}]_2{\cdot}xH_2O$ was significantly better (Figure 8).

The effect coordinated water has on $Mg[CB_{11}H_{12}]_2{\cdot}xH_2O$, $Ca[CB_{11}H_{12}]_2{\cdot}xH_2O$ and $Zn[CB_{11}H_{12}]_2{\cdot}xH_2O$ has to be assessed. Drying $Ca[CB_{11}H_{12}]{\cdot}xH_2O$ and $Zn[CB_{11}H_{12}]_2{\cdot}xH_2O$ at increasingly higher temperatures led to a decrease in the number of coordinated water molecules, for example, for $Ca[CB_{11}H_{12}]_2{\cdot}xH_2O$, when dried at 100 °C, approximately 1.9 equivalents of water could be estimated, whereas drying at 125 °C ~0.8 waters could be identified (Figure 7). Correspondingly, $Zn[CB_{11}H_{12}]_2{\cdot}xH_2O$ had approximately 3 coordinated water molecules when dried at 100 °C, which decreased to ~2 water molecules when dried at 150 °C. Less coordinated water led to

lower ionic conductivities, with $Ca[CB_{11}H_{12}]_2{\cdot}1.9H_2O$ at 100 °C showing an ionic conductivity of 1.9 x 10^{-6} S cm^{-1}, whereas, $Ca[CB_{11}H_{12}]_2{\cdot}0.8H_2O$ had an ionic conductivity of 7.9 x 10^{-8} S cm^{-1} at 100 °C. At 100 °C $Zn[CB_{11}H_{12}]_2{\cdot}3H_2O$ and $Zn[CB_{11}H_{12}]_2{\cdot}2H_2O$ displayed ionic conductivities of 2.7 x 10^{-5} S cm^{-1} and 1.5 x 10^{-7} S cm^{-1}, respectively. This was similar to what has been observed in a recent investigation into the role water plays in the solid-state ionic conductivity of $Mg[B_{12}H_{12}]{\cdot}12H_2O$ and $Zn[B_{12}H_{12}]_2{\cdot}12H_2O$.[78] The effect of high water content in $Mg[B_{12}H_{12}]{\cdot}12H_2O$ allows for room temperature ionic conductivity of ≈ 10^{-6} S cm^{-1} at 30 °C, which is significantly higher compared to other less solvated samples, including $Mg[CB_{11}H_{12}]_2{\cdot}3.1H_2O$ (Figure 6).[78] The decrease in ionic conductivity was also significant for hydrated $Zn[B_{12}H_{12}]$, with a conductivity of ~10^{-4} S cm^{-1} at 60 °C for $Zn[B_{12}H_{12}]{\cdot}12H_2O$, whereas $Zn[B_{12}H_{12}]{\cdot}2.7H_2O$ had no measurable ionic conductivity below 80 °C (Figure 7b).[78] Kisu *et al.,*[78] postulated that the contribution of additional structural water was found to increase the distance between anion and cation, thus, decreasing the coulombic attractive forces between cation and anion. This weaker attraction allowed for easier cation migration via reorientation of the $[B_{12}H_{12}]^{-}$ anion, i.e., the 'paddle-wheel' effect'.[78]

Similarly, the addition of metal oxides to $Mg[BH_4]_2{\cdot}1.5NH_3$, including MgO and TiO_2, increases ionic conductivity at 25 °C (~10^{-5} – 10^{-6} S cm^{-1} for $Mg[BH_4]_2{\cdot}1.5NH_3$@MgO and 3 x 10^{-4} S cm^{-1} for $Mg[BH_4]_2{\cdot}1.5NH_3$ + 60wt% TiO_2).[79,80] Multiple theories exist to explain the increased ionic conductivity due to the formation of nanocomposites. For $Mg[BH_4]_2{\cdot}1.6NH_3$ the addition of 75wt% of MgO stabilises an amorphous phase, which increases the ionic conductivity.[80] Alternatively, TiO_2 addition to $Mg[BH_4]_2{\cdot}1.5NH_3$ was theorised to increase the ionic conductivity due to increased oxygen vacancies on the surface of the metal oxide.[79]

Attempts to measure the stability of $Zn[CB_{11}H_{12}]_2{\cdot}xH_2O$ against Zn metal using LSV proved to be difficult and not reproducible. Despite this issue in the solid-state, there are potential alternative uses for *closo*-monocarboranes that are beyond the scope of this study. For example, $Zn[CB_{11}H_{12}]_2$ could have applications in aqueous polymer batteries. Large, bulky anions, such as $TFSI^-$ or $CF_3SO_3^-$, have already been studied as replacements in these types of batteries, thus, $CB_{11}H_{12}^-$ may also have success. Non-aqueous liquid batteries are another potential use as found in magnesium carborane electrolytes $Mg[CB_{11}H_{12}]_2$ in tetraglyme (0.75 M) which has a ionic conductivity of 10^{-3} S cm^{-1} at room temperature.[13]

Conclusion

Hydrated $Mg[CB_{11}H_{12}]_2{\cdot}xH_2O$, $Ca[CB_{11}H_{12}]_2{\cdot}xH_2O$, and $Zn[CB_{11}H_{12}]_2{\cdot}xH_2O$ show potential as solid-state electrolytes. Solvation aids in improving the ionic conductivity of the different salts. Comparison of the ionic conductivities of $Mg[CB_{11}H_{12}]_2{\cdot}3.1H_2O$, $Ca[CB_{11}H_{12}]_2{\cdot}xH_2O$, and $Zn[CB_{11}H_{12}]_2{\cdot}xH_2O$ indicated that $Ca[CB_{11}H_{12}]_2{\cdot}1.9H_2O$ with no modifications (i.e. ball milling) had the highest ionic conductivity at modest temperatures (< 70 °C), however, $Zn[CB_{11}H_{12}]_2{\cdot}xH_2O$ had significantly higher ionic conductivities at elevated temperature (> 100 °C). Interestingly, thermal analysis of all compounds show a decomposition via a dehydrogenation and hydroxylation mechanism, similar to hydrated samples of $Mg[B_{12}H_{12}]$. Nevertheless, the synthesis and ionic conductivity of $Mg[CB_{11}H_{12}]_2{\cdot}3en$ proved to be higher than that of $Mg[CB_{11}H_{12}]_2{\cdot}3.1H_2O$, yet, it did prove to have a much lower oxidative stability. This study provides a comprehensive thermal analysis of the divalent *closo*-monocarborane salts and opens up further research in the synthesis, characterisation, and development of other solvated metal solid-state electrolytes for battery applications.

Conflicts of interest

There are no conflicts of interest to declare.

Acknowledgements

MP acknowledges Curtin University for his Senior Research Fellowship. We would like to acknowledge the help of Dr Thomas Becker who aided in the collection of Raman spectroscopy. This research was undertaken on the Powder Diffraction beamline at the Australian Synchrotron, part of ANSTO.

Experimental

Chemicals

Sodium hydroxide (NaOH, ≥ 98 %), magnesium hydroxide ($Mg(OH)_2$, ≥ 99 %), magnesium carbonate (basic) ($MgCO_3{\cdot}Mg(OH)_2$, ≥ 40 %), calcium carbonate ($CaCO_3$, > 99 %), zinc carbonate (basic) ($ZnCO_3{\cdot}Zn(OH)_2$, 58 % zinc), concentrated sulfuric acid (H_2SO_4, 95-98 %), anhydrous diethyl ether (Et_2O, ≥99 %), *n*-dibutylmagnesium ($MgBu_2$, 1M, heptane), ethylenediamine ($C_2H_4(NH_2)_2$, (en), ≥ 99 %) and hexane (mixed isomers, C_6H_{14}, anhydrous, ≥ 99 %) were purchased from Merck, as were Amberlyte® IR120 hydrogen form resin ion exchange beads. All aqueous solutions used ultrapure deionised water (18 MΩ.cm).

NMR solvents: deuterated water (D_2O, 99.9 atom% D), deuterated acetone ($(CD_3)_2CO$, 99.9 atom% D), deuterated dimethyl sulfoxide (DMSO-d_6, anhydrous, 99.9 atom% D), and deuterated acetonitrile (CD_3CN, 99.8 atom% D), were purchased from Merck.

For linear sweep voltammetry (LSV): magnesium metal was purchased from Westlab (Mg ribbon, 0.3 mm thickness, 99.5%) and zinc metal foil (0.1 mm thickness) was purchased from ChemSupply. Calcium metal was synthesised from the dehydrogenation of calcium hydride at 800 °C for 10 hours in a sealed stainless steel reactor open to vacuum (CaH_2, Merck, 95 %) and hydraulically pressed to a thickness of approximately 0.1 mm. Platinum foil (Pt, 99.99 %, 0.1 mm) and gold foil (Au, 99.95 %, 0.1 mm) were purchased from Merck, and carbon black (Super P conductive carbon, C, 99+ %) was purchased from

Thermo Fisher Scientific. All metals were polished prior to use by hand in the glovebox using diamond polishing film (6 μm).

Synthesis of $M[CB_{11}H_{12}]_2{\cdot}xH_2O$ (M = Mg, Ca or Zn)

$Me_3NH[CB_{11}H_{12}]$ was synthesised by a previously published method,[53] which was then reacted with aqueous NaOH (1.5 equiv.) at 60 – 80 °C for 1 hour to form a solution of $Na[CB_{11}H_{12}]$. This solution was filtered through a fine frit before it was passed through an hydrogen-form ion exchange column to create the acid form of the *closo*-monocarborane, $[H_3O][CB_{11}H_{12}]$. Excess $Mg(OH)_2$ (or $MgCO_3$), $CaCO_3$, or basic-$ZnCO_3$ was added to this solution and stirred for 2 – 3 hours until the pH was approximately 6. Excess solid was removed using filtration and excess water was distilled using rotary evaporation at 60 °C. The resultant solid was then dried at 100 °C, 125 °C, or 150 °C under vacuum for 16 hours as stated. All samples were stored and handled in an argon filled glovebox (H_2O/O_2 < 1 ppm).
$M[CB_{11}H_{12}]_2{\cdot}xH_2O$ (M = Mg, Ca or Zn); ^{1}H NMR (D_2O, 400 MHz): δ (ppm) 2.28 (s, 1H, CH), 1.70–0.86 (bm, 11H, BH2–12). ^{11}B NMR (D_2O, 128 MHz) δ: −6.9 (d, J = 139.2 Hz, 1B, B12), −13.3 (d, J = 136.9 Hz, 5B, B7–11), −16.2 (d, J = 151.2 Hz, 5B, B2–6). ^{11}B{^{1}H} NMR (D_2O, 128 MHz) δ: −6.9 (1B), −13.3 (5B), −16.2 (5B). FTIR (ATR, 16 scans, cm^{-1}): 3525 – 3450 (bm), 2510 (s), 1602 (s) 1057 (w). (Figure S1 and S8).

Synthesis of $Mg[CB_{11}H_{12}]_2$ and $Mg[CB_{11}H_{12}]_2{\cdot}3en$

An excess amount of *n*-dibutylmagnesium in heptane (2.5 eq., 1 M) was added dropwise to a slurry of $Me_3NH[CB_{11}H_{12}]$ in hexane, whilst cooled in an ice bath and under Ar using Schlenk techniques. A visible change could be identified as the mixture became less yellow in colour as the reaction continued. After 4 hours, the solvent was removed via vacuum and the waxy solid was thoroughly washed with hexane 3 times, leaving a fine white powder, which was dried at 100 °C to remove excess hexane. Care was taken to ensure that no moisture was absorbed by the product by avoiding air exposure and storing the sample in an Ar glovebox. The white powdered product of $Mg[CB_{11}H_{12}]_2$ was mixed with excess ethylenediamine and then dried under vacuum at 100 °C for 1 hour leaving a bright yellow solid that was subsequently stored under argon.
$Mg[CB_{11}H_{12}]_2$; ^{1}H NMR (DMSO-*d6*, 400 MHz): δ (ppm) 2.39 (s), 1.95-0.57 (bm). ^{11}B NMR (DMSO-*d6*, 128 MHz): δ (ppm) -7.0 (d, J = 137.1 Hz, 1B), -13.3 (d, J = 135.6 Hz, 5B), -16.8 (d, J = 150.6 Hz, 5B). ^{11}B{^{1}H} NMR (DMSO-*d6,* 128 MHz) δ (ppm): -7.0 (1B), -13.3 (5B), -16.3 (5B). ^{13}C{^{1}H} NMR (DMSO-*d6*): δ (ppm) 50.9 C-H (cage), 47.4 (unknown). FTIR (ATR, 16 scans, cm^{-1}): 3571 – 3466 (b), 3185 (w), 2951 (w), 2521 (s), 1615 (m), 1466 (w), 1063 (m). (Figures S2-S6, and S10).
$Mg[CB_{11}H_{12}]_2{\cdot}3en$; ^{1}H NMR (DMSO-*d6*, 400 MHz): δ (ppm) 2.39 (s, 1H), 1.95-0.57 (bm, 12H). ^{11}B NMR (DMSO-*d6*, 128 MHz): δ (ppm) -7.0 (d, J = 138.1 Hz, 1B), -13.3 (d, J = 136.5 Hz, 5B), -16.2 (d, J = 151.6 Hz, 5B). ^{11}B{^{1}H} NMR (DMSO-*d6,* 128 MHz) δ (ppm): -7.1 (1B), -13.3 (5B), -16.3 (5B. ^{13}C{^{1}H} NMR (DMSO-*d6*): δ (ppm) 50.9 (C-H (cage)), 42.8 (en). FTIR (ATR, 16 scans, cm^{-1}): 3677 – 3606 (w), 3337 (m), 3289 (m), 2937 (m) 2890 (w), 2521 (s), 1589 (m), 1463 (w), 1006 (s), 959 (m). (Figures S2-S4, S7 and S10).

Synthesis of $Ca[B_{12}H_{12}]_2{\cdot}xH_2O$ and $Zn[B_{12}H_{12}]_2{\cdot}xH_2O$

$Et_3NH[B_{12}H_{12}]$ was synthesised in a previously described method.[17] This was then converted to $Zn[B_{12}H_{12}]{\cdot}xH_2O$ or $Ca[B_{12}H_{12}]{\cdot}xH_2O$ in the same method as described for the synthesis of $M[CB_{11}H_{12}]_2{\cdot}xH_2O$ (where M = Mg, Ca, or Zn).
$Ca[B_{12}H_{12}]{\cdot}xH_2O$; ^{1}H NMR ($D_2O$, 400 MHz): δ (ppm) 1.66-0.75 (bm, 12H). ^{11}B NMR (D_2O, 128 MHz): δ (ppm) -15.4 (d, J = 125.8 Hz, 12B). ^{11}B{^{1}H} NMR (128 MHz, D_2O) δ (ppm): -15.4 (12B). (Figures S20 and S21).
$Zn[B_{12}H_{12}]{\cdot}xH_2O$; ^{1}H NMR ($CD_3CN$, 400 MHz): δ (ppm) 1.24-0.32 (bm, 12H). ^{11}B NMR (CD_3CN, 128 MHz): δ (ppm) -15.3 (d, J = 124.2 Hz, 12B). ^{11}B{^{1}H} NMR (128 MHz, CD3CN) δ (ppm): -15.3 (12B). (Figures S22 and S23).

Preparation of composite $Zn[B_{12}H_{12}]$-$Zn[CB_{11}H_{12}]_2$ samples

Composite $Zn[B_{12}H_{12}]$-$Zn[CB_{11}H_{12}]_2$ samples were prepared by either ball milling or precipitating stoichiometric amounts of $Zn[B_{12}H_{12}]$ and $Zn[CB_{11}H_{12}]_2$. For example, in the sample $0.7Zn[B_{12}H_{12}]{\cdot}xH_2O$-$0.3Zn[CB_{11}H_{12}]_2{\cdot}xH_2O$-BM, 0.7 molar equivalents of $Zn[B_{12}H_{12}]{\cdot}xH_2O$ and 0.3 molar equivalents of $Zn[CB_{11}H_{12}]_2{\cdot}xH_2O$ were milled in a stainless steel planetary ball mill (Across Industries) under an argon atmosphere for 1 hour using 6 mm balls and a ball to sample mass ratio of 33:1. Alternatively, the sample $0.7Zn[B_{12}H_{12}]{\cdot}xH_2O$-$0.3Zn[CB_{11}H_{12}]_2{\cdot}xH_2O$ was prepared by dissolving 0.7 molar equivalents of $Zn[B_{12}H_{12}]{\cdot}xH_2O$ and 0.3 molar equivalents of $Zn[CB_{11}H_{12}]_2{\cdot}xH_2O$ in deionised water followed by drying for 16 hours at 100 °C under vacuum.
$0.7Zn[B_{12}H_{12}]{\cdot}xH_2O$-$0.3Zn[CB_{11}H_{12}]_2{\cdot}xH_2O$; ^{1}H NMR ($CD_3CN$, 400 MHz): δ (ppm) 1.50-0.52 (bm). ^{11}B NMR (CD_3CN, 128 MHz): δ (ppm) -7.0, -13.3, -14.9 to -16.8. ^{11}B{^{1}H} NMR (128 MHz, CD_3CN) δ (ppm): -7.0, -13.3, -15.4, -16.1. (Figures S24 – S26).
$0.7Zn[B_{12}H_{12}]{\cdot}xH_2O$-$0.3Zn[CB_{11}H_{12}]_2{\cdot}xH_2O$-BM; ^{1}H NMR ($CD_3CN$, 400 MHz): δ (ppm) 1.80-0.56 (bm). ^{11}B NMR (CD_3CN, 128 MHz): δ (ppm) -7.0, -13.3, -14.9 to -16.8. ^{11}B{^{1}H} NMR (128 MHz, CD_3CN) δ (ppm): -6.9, -13.3, -15.3, -16.1. (Figures S24 – S26).
$0.5Zn[B_{12}H_{12}]{\cdot}xH_2O$-$0.5Zn[CB_{11}H_{12}]_2{\cdot}xH_2O$-BM; ^{1}H NMR ($CD_3CN$, 400 MHz): δ (ppm) 1.48-0.56 (bm). ^{11}B NMR (CD_3CN, 128 MHz): δ (ppm) -7.0, -13.3, -14.8 to -16.8. ^{11}B{^{1}H} NMR (128 MHz, CD_3CN) δ (ppm): -7.0, -13.3, -15.3, -16.2. (Figures S24 – S26).
$0.3Zn[B_{12}H_{12}]{\cdot}xH_2O$-$0.7Zn[CB_{11}H_{12}]_2{\cdot}xH_2O$-BM; ^{1}H NMR ($CD_3CN$, 400 MHz): δ (ppm) 1.79-0.58 (bm). ^{11}B NMR (CD_3CN, 128 MHz): δ (ppm) -6.9, -13.3, -14.8 to -16.8. ^{11}B{^{1}H} NMR (128 MHz, CD_3CN) δ (ppm): -6.9, -13.3, -15.3, -16.2. (Figures S24 – S26).

Synthesis of $Me_3NH[12\text{-}OH\text{-}CB_{11}H_{11}]$

Following the method described by Grüner *et al*.,[62] $Na[CB_{11}H_{12}]$ (0.3 g) was mixed with 7 mL H_2SO_4 (80 %) and stirred for 5 hours at 175 - 180 °C. Following this, the reaction was quenched with 10 mL water and cooled to room temperature. The cooled solution was added to 20 mL of water and the product was extracted with Et_2O (3 × 10 mL) and was then mixed with 10 mL water. The Et_2O was removed under vacuum leaving a brown aqueous layer, with solid that was removed via filtration. To this solution, Me_3NHCl was added, and a precipitate was formed.

This solid was filtered and the final product was dried under vacuum at 120 °C.

$Me_3NH[12\text{-}OH\text{-}CB_{11}H_{11}]$; ^1H NMR ($(CD_3)_2CO$, 400MHz): δ (ppm) 8.99 (bs, $NMe_3\mathbf{H}^+$), 3.01 (s, $\mathbf{Me_3}NH^+$), 2.78 (HDO), 2.10 (s, 1H, CH), 2.00-0.75 (bm, 10H, BH). ^{11}B NMR ($(CD_3)_2CO$, 128 MHz): δ (ppm) 11.0 (s, 1B), -14.1 (d, 5B), -18.9 (d, 5B). $^{11}B\{^1H\}$ NMR ($(CD_3)_2CO$, 128 MHz): δ (ppm) 11.0, -14.1, -18.9. (Figures S27 and S28).

Characterisation

Nuclear Magnetic Resonance (NMR) spectra (^1H, $^1H\{^{11}B\}$, ^{11}B, $^{13}C\{^1H\}$) were collected on a Bruker Avance III 400 MHz NanoBay spectrometer at room temperature. The ^{11}B NMR spectra were referenced to a boron trifluoride etherate ($BF_3O(C_2H_5)_2$) external standard, and the ^1H and $^{13}C\{^1H\}$ spectra were referenced to a tetramethylsilane ($Si(CH_3)_4$) external standard. Powdered samples were dissolved in 600 µL of deuterated acetonitrile (CD_3CN), deuterated dimethyl sulfoxide (DMSO-*d6*) deuterated acetone ($(CD_3)_2CO$) or water (D_2O) prior to analysis. Fourier transform infrared spectroscopy (FTIR) was recorded using a Thermo Scientific Nicolet Summit FTIR spectrometer equipped with a diamond attenuated total reflectance (ATR) stage in air at room temperature with a range of 400 – 4000 cm^{-1} using 16 scans.

Raman spectra were collected using a WITec Alpha 300 SAR confocal Raman microscope using a 532 nm green light excitation wavelength and 600 grating/mm. Samples were prepared in an Ar-filled glovebox (H_2O/O_2 < 1 ppm) in 1 mm wide borosilicate capillaries (0.01 mm thick walls) and flamed sealed to prevent air exposure. Spectra were collected with 100 accumulations and an integration time of 400 ms. Background subtraction and data processing was performed using Project 4 (WITec) software.

Powder X-ray diffraction (pXRD) patterns were collected using a Bruker D8 Advance using a CuKα radiation source (λ = 1.5406 Å) in Bragg-Brentano geometry using flat plate holders. Data were collected from 5 – 60° 2ϑ at 0.02° steps over 1 hour. To avoid issues surrounding the deliquescent nature of the divalent salts, a poly(methyl methacrylate) air-tight dome sample holder was used, and samples were prepared for analysis in an Ar-filled glovebox. $Me_3NH[CB_{11}H_{12}]$ was prepared in air with a standard pXRD holder.

Synchrotron powder X-ray diffraction (SR-XRD) patterns were collected for the $Mg[CB_{11}H_{12}]_2$ and $Mg[CB_{11}H_{12}]_2{\cdot}3en$ samples at the Australian Synchrotron using a Mythen microstrip detector. Data were collected from 5 – 50° 2ϑ. The energy of the X-ray beam was 16 keV (λ = 0.774954(1) Å) and refined using a NIST LaB_6 standard (660b). The powder samples were packed and sealed in thick-wall quartz capillaries (0.5 mm inner diameter, 0.1 mm wall thickness) in an Ar-filled glove box to avoid air and moisture exposure. A Serpentine hot air blower was used to heat the samples from RT – 500 °C at 8 °C/min under vacuum. Structural indexing and crystal structure solution was undertaken in Topas software (Bruker, v.5).

Differential scanning calorimetry-thermogravimetric analysis (DSC-TGA) was performed using a NETZSCH STA 449 F3 Jupiter equipped with a platinum furnace. Approximately 3 – 5 mg of sample was placed in aluminium (Al) pans in an Ar-filled glovebox and cold welded to prevent exposure to air. Before analysis, the sample pan lids were pierced and loaded into the instrument and vacuum was directly applied to ensure all air was removed from the furnace before analysis. Analysis was performed under a constant flow of argon (40 mL/min) with a heating rate of 10 °C/min.

A Stanford Research Systems (SRS) residual gas analysis mass spectrometer (RGA-MS) consisting of a quadrupole probe was used to analyse the gases released from the sample as it was heated, data was collected with a mass on charge ratio of 65 AMU. For this, approximately 2 mg of sample was placed in a Swagelok reactor, which was then placed into a tube furnace. A ramp rate of 10 °C/min was used from 30 – 350 °C, with a vacuum pressure of approximately 10^{-4} mbar.

Temperature programmable photographic analysis (TPPA) of powder pellets was used to visualise the physical changes that occurred as a sample was heated.[81] A pellet of approximately 30 – 50 mg was put in a borosilicate test tube which was sealed in a glovebox using a rubber septa. An Ar-filled balloon was inserted into the septa to maintain an Ar-atmosphere and a thermocouple was placed inside the tube, through the septa and next to the pellet, to measure temperature. The sample was heated at a rate of 4 °C/min from 25 °C – 350 °C.

Electrochemical impedance spectrometry (EIS) was performed using a ZIVELab SP1 potentiostat to determine the ionic conductivity of the different salts. Pellets were prepared in an Ar-filled glovebox using a 6 mm diameter die, pressed between 0.1 mm thick gold foils at a pressure of 700 MPa. The pellets were then placed in air-tight Swagelok-type Teflon cells with 316 stainless steel electrodes gently pressed together with a spring. EIS was carried out at 50 mV AC, from 10 Hz to 1 MHz, at temperatures ranging from room temperature to 190 °C at 10 °C intervals. Temperature was controlled using a tube furnace and monitored using a K-type thermocouple. Samples were left to thermally equilibrate at the set temperature for 30 minutes before EIS was conducted. Ionic conductivity was then calculated from Nyquist plots using the following equation;

$$\sigma = \frac{d}{IA}$$

where σ is ionic conductivity (S cm^{-1}), d is pellet thickness (cm), A is the area of the pellet (cm^2) and I is the intercept of the semicircle and/or linear diffusion controlled region with the x-axis, indicating the electrolyte resistance.[76] A sample of Nyquist plots used to calculate ionic conductivity are located in the supplementary information (Figures S29 - S32).

Linear sweep voltammetry (LSV) was used to investigate the oxidative stability of the hydrated divalent salts ($Mg(CB_{11}H_{12})_2{\cdot}xH_2O$, $Ca(CB_{11}H_{12})_2{\cdot}xH_2O$ and $Zn(CB_{11}H_{12})_2{\cdot}xH_2O$) against their respective metals based on previously determined methods.[18,48,72] Solid electrolyte powder was mixed with Super-P conductive carbon (TIMCAL) in a weight ratio of 75:25 and ground in a mortar and pestle 5 times to make a composite material to increase electronic contact between electrolyte and current collector.[72] To prepare the composite pellet, a 6 mm

diameter metal foil (Mg, Ca, or Zn) was cut and placed in a 6 mm diameter die. On top of this, 40 mg of electrolyte was placed followed by 2.5 mg of the electrolyte/C composite, which was layered on top. This was pressed at a pressure of 350 MPa and was placed in an air-tight Swagelok-type Teflon cell in an Al/Pt/composite/sample/*M* (*M* = Mg, Ca, or Zn) configuration. As the samples are poor ionic conductors at low temperatures, the samples were measured at 100 °C, with a scan rate or 50 μV s^{-1} from 0 – 6 V. The oxidative stability was calculated from the linear intercept of the background current with the oxidative current onset.

References

1 N. Nitta, F. Wu, J. T. Lee and G. Yushin, Li-ion battery materials: present and future, *Mater. Today*, 2015, **18**, 252–264.

2 P. W. Gruber, P. A. Medina, G. A. Keoleian, S. E. Kesler, M. P. Everson and T. J. Wallington, Global lithium availability: A constraint for electric vehicles?, *J. Ind. Ecol.*, 2011, **15**, 760–775.

3 H. Ye and Y. Li, Review on Multivalent Rechargeable Metal–Organic Batteries, *Energy & Fuels*, 2021, **35**, 7624–7636.

4 L. F. O'Donnell and S. G. Greenbaum, Review of Multivalent Metal Ion Transport in Inorganic and Solid Polymer Electrolytes, *Batteries*, 2020, **7**, 3.

5 A. Ponrouch, J. Bitenc, R. Dominko, N. Lindahl, P. Johansson and M. R. Palacin, *Energy Storage Mater.*, 2019, 20, 253–262.

6 A. Ponrouch and M. Rosa Palacín, *Philos. Trans. R. Soc. A Math. Phys. Eng. Sci.*, 2019, 377.

7 Y. T. Lu, A. R. Neale, C. C. Hu and L. J. Hardwick, Divalent Nonaqueous Metal-Air Batteries, *Front. Energy Res.*, 2021, **8**, 357.

8 Y. Liang, H. Dong, D. Aurbach and Y. Yao, Current status and future directions of multivalent metal-ion batteries, *Nat. Energy 2020 59*, 2020, **5**, 646–656.

9 J. Muldoon, C. B. Bucur and T. Gregory, *Chem. Rev.*, 2014, 114, 11683–11720.

10 R. Jay, A. W. Tomich, J. Zhang, Y. Zhao, A. De Gorostiza, V. Lavallo and J. Guo, Comparative Study of Mg(CB 11 H 12) 2 and Mg(TFSI) 2 at the Magnesium/Electrolyte Interface, *ACS Appl. Mater. Interfaces*, 2019, **11**, 11414–11420.

11 I. Shterenberg, M. Salama, H. D. Yoo, Y. Gofer, J.-B. Park, Y.-K. Sun and D. Aurbach, Evaluation of (CF 3 SO 2) 2 N – (TFSI) Based Electrolyte Solutions for Mg Batteries, *J. Electrochem. Soc.*, 2015, **162**, A7118–A7128.

12 J. Luo, Y. Bi, L. Zhang, X. Zhang and T. L. Liu, A Stable, Non-Corrosive Perfluorinated Pinacolatoborate Mg Electrolyte for Rechargeable Mg Batteries, *Angew. Chemie*, 2019, **131**, 7041–7045.

13 O. Tutusaus, R. Mohtadi, T. S. Arthur, F. Mizuno, E. G. Nelson and Y. V. Sevryugina, An Efficient Halogen-Free Electrolyte for Use in Rechargeable Magnesium Batteries, *Angew. Chemie*, 2015, **127**, 8011–8015.

14 K. Kisu, S. Kim, T. Shinohara, K. Zhao, A. Züttel and S. Orimo, Monocarborane cluster as a stable fluorine-free calcium battery electrolyte, *Sci. Rep.*, 2021, **11**, 1–8.

15 B. Huang, B. Xu, Y. Li, W. Zhou, Y. You, S. Zhong, C. A. Wang and J. B. Goodenough, Li-Ion Conduction and Stability of Perovskite Li3/8Sr7/16Hf1/4Ta3/4O3, *ACS Appl. Mater. Interfaces*, 2016, **8**, 14552–14557.

16 Y. Li, J. T. Han, C. A. Wang, H. Xie and J. B. Goodenough, Optimizing Li+ conductivity in a garnet framework, *J. Mater. Chem.*, 2012, **22**, 15357–15361.

17 B. R. S. Hansen, M. Paskevicius, H. W. Li, E. Akiba and T. R. Jensen, *Coord. Chem. Rev*, 2016, 323, 60–70.

18 D. H. P. Souza, K. T. Møller, S. A. Moggach, T. D. Humphries, A. M. D'Angelo, C. E. Buckley and M. Paskevicius, Hydrated alkali-B11H14 salts as potential solid-state electrolytes, *J. Mater. Chem. A*, 2021, **9**, 15027–15037.

19 M. Jørgensen, S. R. H. Jensen, T. D. Humphries, M. R. Rowles, M. V Sofianos, C. E. Buckley, T. R. Jensen and M. Paskevicius, Hydroxylated closo-Dodecaborates M2B12(OH)12(M = Li, Na, K, and Cs); Structural Analysis, Thermal Properties, and Solid-State Ionic Conductivity, *J. Phys. Chem. C*, 2020, **124**, 11340–11349.

20 S. Ikeda, M. Takahashi, J. Ishikawa and K. Ito, Solid electrolytes with multivalent cation conduction. 1. Conducting species in MgZrPO4 system, *Solid State Ionics*, 1987, **23**, 125–129.

21 S. Tamura, M. Yamane, Y. Hoshino and N. Imanaka, Highly conducting divalent Mg2+ cation solid electrolytes with well-ordered three-dimensional network structure, *J. Solid State Chem.*, 2016, **235**, 7–11.

22 Y. Zhan, W. Zhang, B. Lei, H. Liu and W. Li, *Front. Chem.*, 2020, 8, 125.

23 R. Le Ruyet, B. Fleutot, R. Berthelot, Y. Benabed, G. Hautier, Y. Filinchuk and R. Janot, Mg3(BH4)4(NH2)2as Inorganic Solid Electrolyte with High Mg2+Ionic Conductivity, *ACS Appl. Energy Mater.*, 2020, **3**, 6093–6097.

24 R. Mohtadi, M. Matsui, T. S. Arthur and S. J. Hwang, Magnesium borohydride: From hydrogen storage to magnesium battery, *Angew. Chemie - Int. Ed.*, 2012, **51**, 9780–9783.

25 K. Kisu, S. Kim, M. Inukai, H. Oguchi, S. Takagi and S. I. Orimo, Magnesium Borohydride Ammonia Borane as a Magnesium Ionic Conductor, *ACS Appl. Energy Mater.*, 2020, **3**, 3174–3179.

26 E. Roedern, R. S. Kühnel, A. Remhof and C. Battaglia, Magnesium Ethylenediamine Borohydride as Solid-State Electrolyte for Magnesium Batteries, *Sci. Rep.*, 2017, **7**, 46189.

27 S. Higashi, K. Miwa, M. Aoki and K. Takechi, A novel inorganic solid state ion conductor for rechargeable Mg batteries, *Chem. Commun.*, 2014, **50**, 1320–1322.

28 K. Nomura, S. Ikeda, K. Ito and H. Einaga, Framework Structure, Phase Transition, and Transport Properties in M II Zr 4 (PO 4) 6 Compounds (M II = Mg, Ca, Sr, Ba, Mn, Co, Ni, Zn, Cd, and Pb), *Bull. Chem. Soc. Jpn.*, 1992, **65**, 3221–3227.

29 W. Lee, S. Tamura and N. Imanaka, Synthesis and

characterization of divalent ion conductors with NASICON-type structures, *J. Asian Ceram. Soc.*, 2019, **7**, 221–227.

30 S. Ikeda, Y. Kanbayashi, K. Nomura, A. Kasai and K. Ito, Solid electrolytes with multivalent cation conduction (2) zinc ion conduction in ZnZrPO4 system, *Solid State Ionics*, 1990, **40**–**41**, 79–82.

31 A. J. Martinolich, C. W. Lee, I. Te Lu, S. C. Bevilacqua, M. B. Preefer, M. Bernardi, A. Schleife and K. A. See, Solid-State Divalent Ion Conduction in ZnPS3, *Chem. Mater.*, 2019, **31**, 3652–3661.

32 S. P. Candhadai Murali and A. S. Samuel, Zinc ion conducting blended polymer electrolytes based on room temperature ionic liquid and ceramic filler, *J. Appl. Polym. Sci.*, 2019, **136**, 47654.

33 Y. Huang, J. Zhang, J. Liu, Z. Li, S. Jin, Z. Li, S. Zhang and H. Zhou, Flexible and stable quasi-solid-state zinc ion battery with conductive guar gum electrolyte, *Mater. Today Energy*, 2019, **14**, 100349.

34 K. Wu, J. Huang, J. Yi, X. Liu, Y. Liu, Y. Wang, J. Zhang and Y. Xia, Recent Advances in Polymer Electrolytes for Zinc Ion Batteries: Mechanisms, Properties, and Perspectives, *Adv. Energy Mater.*, 2020, **10**, 1903977.

35 D. Xu, H. Zhang, Z. Cao, L. Wang, Z. Ye, B. Chen, X. Li, X. Zhu, M. Ye and J. Shen, High-rate aqueous zinc-ion batteries enabled by a polymer/graphene composite cathode involving reversible electrolyte anion doping/dedoping, *J. Mater. Chem. A*, 2021, **9**, 10666–10671.

36 J. Han, Z. Chen and J. Xu, A novel electrolyte study on polyaniline aqueous zinc-ion battery, *Mater. Lett.*, 2021, **304**, 130629.

37 Y. Zhao, Y. Huang, F. Wu, R. Chen, L. Li, Y. Zhao, Y. Huang, F. Wu, R. Chen and L. Li, High-Performance Aqueous Zinc Batteries Based on Organic/Organic Cathodes Integrating Multiredox Centers, *Adv. Mater.*, 2021, **33**, 2106469.

38 T. Yao, F. S. Genier, S. Biria and I. D. Hosein, A solid polymer electrolyte for aluminum ion conduction, *Results Phys.*, 2018, **10**, 529–531.

39 T. Leisegang, F. Meutzner, M. Zschornak, W. Münchgesang, R. Schmid, T. Nestler, R. A. Eremin, A. A. Kabanov, V. A. Blatov and D. C. Meyer, The aluminum-ion battery: A sustainable and seminal concept?, *Front. Chem.*, 2019, **7**, 268.

40 F. S. Genier, C. V. Burdin, S. Biria and I. D. Hosein, A novel calcium-ion solid polymer electrolyte based on crosslinked poly(ethylene glycol) diacrylate, *J. Power Sources*, 2019, **414**, 302–307.

41 S. Huang, J. Zhu, J. Tian and Z. Niu, Recent Progress in the Electrolytes of Aqueous Zinc-Ion Batteries, *Chem. – A Eur. J.*, 2019, **25**, 14480–14494.

42 S. G. McArthur, R. Jay, L. Geng, J. Guo and V. Lavallo, Below the 12-vertex: 10-vertex carborane anions as non-corrosive, halide free, electrolytes for rechargeable Mg batteries, *Chem. Commun.*, 2017, **53**, 4453–4456.

43 A. V. Skripov, R. V. Skoryunov, A. V. Soloninin, O. A. Babanova, W. S. Tang, V. Stavila and T. J. Udovic, Anion Reorientations and Cation Diffusion in $LiCB_{11}H_{12}$ and $NaCB_{11}H_{12}$: ^{1}H, ^{7}Li, and ^{23}Na NMR Studies, *J. Phys. Chem. C*, 2015, **119**, 26912–26918.

44 M. Dimitrievska, P. Shea, K. E. Kweon, M. Bercx, J. B. Varley, W. S. Tang, A. V. Skripov, V. Stavila, T. J. Udovic and B. C. Wood, Carbon Incorporation and Anion Dynamics as Synergistic Drivers for Ultrafast Diffusion in Superionic LiCB11H12 and NaCB11H12, *Adv. Energy Mater.*, 2018, **8**, 1–10.

45 M. Brighi, F. Murgia and R. Černý, Closo-Hydroborate Sodium Salts as an Emerging Class of Room-Temperature Solid Electrolytes, *Cell Reports Phys. Sci.*, 2020, **1**, 100217.

46 U.S. Geological Survery, *Mineral commodity summaries 2022*, Reston, VA, 2022.

47 M. Brighi, F. Murgia, Z. Łodziana, P. Schouwink, A. Wołczyk and R. Černý, A mixed anion hydroborate/carba-hydroborate as a room temperature Na-ion solid electrolyte, *J. Power Sources*, 2018, **404**, 7–12.

48 R. Asakura, D. Reber, L. Duchêne, S. Payandeh, A. Remhof, H. Hagemann and C. Battaglia, 4 V Room-Temperature All-Solid-State Sodium Battery Enabled By a Passivating Cathode/Hydroborate Solid Electrolyte Interface, *Energy Environ. Sci.*, 2020, **13**, 5048–5058.

49 R. J. Wiersema and M. F. Hawthorne, Electrochemistry and Boron-11 Nuclear Magnetic Resonance Spectra of Monocarbon Carboranes, *Inorg. Chem.*, 1973, **12**, 785–788.

50 S. Körbe, P. J. Schreiber and J. Michl, Chemistry of the Carba-closo-dodecaborate(-) anion, CB11H12-, *Chem. Rev.*, 2006, **106**, 5208–5249.

51 L. Toom, A. Kütt and I. Leito, Simple and scalable synthesis of the carborane anion CB11H12-, *Dalt. Trans.*, 2019, **48**, 7499–7502.

52 J. Pecyna, I. Rončević and J. Michl, Insertion of Carbenes into Deprotonated nido-Undecaborane, B11H13(2-), *Molecules*, 2019, **24**, 1–13.

53 A. Berger, C. E. Buckley and M. Paskevicius, Synthesis of closo-CB11H12-Salts Using Common Laboratory Reagents, *Inorg. Chem.*, 2021, **60**, 14744–14751.

54 X. Chen, Y.-H. H. Liu, A.-M. M. Alexander, J. C. Gallucci, S.-J. J. Hwang, H. K. Lingam, Z. Huang, C. Wang, H. Li, Q. Zhao, U. S. Ozkan, S. G. Shore and J.-C. C. Zhao, Desolvation and Dehydrogenation of Solvated Magnesium Salts of Dodecahydrododecaborate: Relationship between Structure and Thermal Decomposition, *Chem. – A Eur. J.*, 2014, **20**, 7325–7333.

55 X. Chen, H. K. Lingam, Z. Huang, T. Yisgedu, J. C. Zhao and S. G. Shore, Thermal decomposition behavior of hydrated magnesium dodecahydrododecaborates, *J. Phys. Chem. Lett.*, 2010, **1**, 201–204.

56 S. G. McArthur, L. Geng, J. Guo and V. Lavallo, Cation reduction and comproportionation as novel strategies to produce high voltage, halide free, carborane based electrolytes for rechargeable Mg batteries, *Inorg. Chem. Front.*, 2015, **2**, 1101–1104.

57 R. J. Abraham and M. Mobli, *Modelling H NMR Spectra of Organic Compounds: Theory, Applications and NMR Prediction Software*, Wiley, Chichester, 2008.

58 S. P. Fisher, A. W. Tomich, S. O. Lovera, J. F. Kleinsasser, J.

Guo, M. J. Asay, H. M. Nelson and V. Lavallo, Nonclassical Applications of closo-Carborane Anions: From Main Group Chemistry and Catalysis to Energy Storage, *Chem. Rev.*, 2019, **119**, 8262–8290.

59 W. S. Tang, A. Unemoto, W. Zhou, V. Stavila, M. Matsuo, H. Wu, S. Orimo and T. J. Udovic, Unparalleled lithium and sodium superionic conduction in solid electrolytes with large monovalent cage-like anions, *Energy Environ. Sci.*, 2015, **8**, 3637–3645.

60 J. Chen, Y. S. Chua, H. Wu, Z. Xiong, T. He, W. Zhou, X. Ju, M. Yang, G. Wu and P. Chen, Synthesis, structures and dehydrogenation of magnesium borohydride–ethylenediamine composites, *Int. J. Hydrogen Energy*, 2015, **40**, 412–419.

61 A. K. Galwey and G. M. Laverty, The thermal decomposition of magnesium chloride dihydrate, *Thermochim. Acta*, 1989, **138**, 115–127.

62 B. Grüner, I. Císařová, J. Čáslavský, B. Bonnetot and D. Cornu, Synthesis of 12-hydroxy and 12-dioxane derivatives of the closo-1-carbadodecaborate(1-) ion. Variations on the plešek's cobalt bis(dicarbollide) pattern, *Collect. Czechoslov. Chem. Commun.*, 2002, **67**, 953–964.

63 T. Peymann, C. B. Knobler and M. F. Hawthorne, A Study of the Sequential Acid-Catalyzed Hydroxylation of Dodecahydro-closo-dodecaborate(2-), *Inorg. Chem.*, , DOI:10.1021/ic991105.

64 M. L. McKee, Computed properties of the CB9H10 and CB11H12 free radicals, *J. Am. Chem. Soc.*, 1997, **119**, 4220–4223.

65 F. Teixidor, C. Viñas and R. W. Rudolph, Rules for Predicting the 11B NMR Spectra of closo-Boranes and closo-Heteroboranes, *Inorg. Chem.*, 1986, **25**, 3339–3345.

66 K. T. Møller, M. Paskevicius, J. G. Andreasen, J. Lee, N. Chen-Tan, J. Overgaard, S. Payandeh, D. S. Silvester, C. E. Buckley and T. R. Jensen, Molten metal closo-borate solvates, *Chem. Commun.*, 2019, **55**, 3410–3413.

67 V. Stavila, J. H. Her, W. Zhou, S. J. Hwang, C. Kim, L. A. M. Ottley and T. J. Udovic, Probing the structure, stability and hydrogen storage properties of calcium dodecahydro-closo-dodecaborate, *J. Solid State Chem.*, 2010, **183**, 1133–1140.

68 R. D. Shannon, Revised effective ionic radii and systematic studies of interatomic distances in halides and chalcogenides, *Acta Crystallogr. Sect. A*, 1976, **32**, 751–767.

69 M. Heere, A. L. Hansen, S. H. Payandeh, N. Aslan, G. Gizer, M. H. Sørby, B. C. Hauback, C. Pistidda, M. Dornheim and W. Lohstroh, Dynamics of porous and amorphous magnesium borohydride to understand solid state Mg-ion-conductors, *Sci. Rep.*, 2020, **10**, 1–11.

70 T. Burankova, E. Roedern, A. E. Maniadaki, H. Hagemann, D. Rentsch, Z. Lodziana, C. Battaglia, A. Remhof and J. P. Embs, Dynamics of the Coordination Complexes in a Solid-State Mg Electrolyte, *J. Phys. Chem. Lett.*, 2018, **9**, 6450–6455.

71 L. P. Wang, Z. Zhao-Karger, F. Klein, J. Chable, T. Braun, A. R. Schür, C. R. Wang, Y. G. Guo and M. Fichtner, MgSc2Se4—A Magnesium Solid Ionic Conductor for All-Solid-State Mg Batteries?, *ChemSusChem*, 2019, **12**, 2286–2293.

72 R. Asakura, L. Duchêne, R. S. Kühnel, A. Remhof, H. Hagemann and C. Battaglia, Electrochemical Oxidative Stability of Hydroborate-Based Solid-State Electrolytes, *ACS Appl. Energy Mater.*, 2019, **2**, 6924–6930.

73 M. Joos, C. Schneider, A. Münchinger, I. Moudrakovski, R. Usiskin, J. Maier and B. V Lotsch, Impact of hydration on ion transport in Li2Sn2S5·xH2O, *J. Mater. Chem. A*, 2021, **9**, 16532–16544.

74 Y. Yu, A. Baskin, C. Valero-Vidal, N. T. Hahn, Q. Liu, K. R. Zavadil, B. W. Eichhorn, D. Prendergast and E. J. Crumlin, Instability at the electrode/electrolyte interface induced by hard cation chelation and nucleophilic attack, *Chem. Mater.*, 2017, **29**, 8504–8512.

75 F. Murgia, M. Brighi, L. Piveteau, C. E. Avalos, V. Gulino, M. C. Nierstenhöfer, P. Ngene, P. De Jongh and R. Černý, Enhanced Room-Temperature Ionic Conductivity of NaCB11H12via High-Energy Mechanical Milling, *ACS Appl. Mater. Interfaces*, 2021, **13**, 61346–61356.

76 B. R. S. Hansen, M. Paskevicius, M. Jørgensen and T. R. Jensen, Halogenated Sodium-closo-Dodecaboranes as Solid-State Ion Conductors, *Chem. Mater.*, 2017, **29**, 3423–3430.

77 T. J. Udovic, M. Matsuo, A. Unemoto, N. Verdal, V. Stavila, A. V. Skripov, J. J. Rush, H. Takamura and S. I. Orimo, Sodium superionic conduction in Na2B12H12, *Chem. Commun.*, 2014, **50**, 3750–3752.

78 K. Kisu, A. Dorai, S. Kim, R. Hamada, A. Kumatani, Y. Horiguchi, R. Sato, K. Sau, S. Takagi and S. I. Orimo, Fast divalent conduction in MB12H12·12H2O (M = Zn, Mg) complex hydrides: effects of rapid crystal water exchange and application for solid-state electrolytes, *J. Mater. Chem. A*, 2022, **10**, 24877–24887.

79 Q. Wang, H. Li, R. Zhang, Z. Liu, H. Deng, W. Cen, Y. Yan and Y. Chen, Oxygen vacancies boosted fast Mg2+ migration in solids at room temperature, *Energy Storage Mater.*, 2022, **51**, 630–637.

80 Y. Yan, J. B. Grinderslev, M. Jo rgensen, L. N. Skov, J. rgen Skibsted and T. R. Jensen, Ammine Magnesium Borohydride Nanocomposites for All-Solid-State Magnesium Batteries, *ACS Appl. Energy Mater.*, 2020, **3**, 9264–9270.

81 M. B. Ley, M. Paskevicius, P. Schouwink, B. Richter, D. A. Sheppard, C. E. Buckley and T. R. Jensen, Novel solvates M(BH 4) 3 S(CH 3) 2 and properties of halide-free M(BH 4) 3 (M = Y or Gd), *Dalt. Trans.*, 2014, **43**, 13333–13342.